**Astronomy
&
Astrophysics**

Pulsation tomography of rapidly oscillating Ap stars[*,**]

Resolving the third dimension in peculiar pulsating stellar atmospheres

T. Ryabchikova[1,2], M. Sachkov[2], O. Kochukhov[3], and D. Lyashko[4]

[1] Department of Astronomy, University of Vienna, Türkenschanzstrasse 17, 1180 Wien, Austria
[2] Institute of Astronomy, Russian Academy of Sciences, Pyatnitskaya 48, 119017 Moscow, Russia
   e-mail: ryabchik@inasan.ru
[3] Department of Astronomy and Space Physics, Uppsala University Box 515, 75120 Uppsala, Sweden
[4] Tavrian National University, Yaltinskaya 4, 330000 Simferopol, Ukraine

ABSTRACT

Aims. We present detailed analysis of the vertical pulsation mode cross-section in ten rapidly oscillating Ap (roAp) stars based on spectroscopic time-series observations. The aim of this analysis is to derive from observations a complete picture of how the amplitude and phase of magnetoacoustic waves depend on depth.

Methods. We use the unique properties of roAp stars, in particular chemical stratification, to resolve the vertical structure of p-modes. Our approach consists of characterising pulsational behaviour of a carefully chosen, but extensive sample of spectral lines. We analyse the resulting amplitude-phase diagrams and interpret observations in terms of pulsation wave propagation.

Results. We find common features in the pulsational behaviour of roAp stars. Within a sample of representative elements the lowest amplitudes are detected for Eu II (and Fe in 33 Lib and in HD 19918), then pulsations go through the layers where Hα core, Nd, and Pr lines are formed. There RV amplitude reaches its maximum, and after that decreases in most stars. The maximum RV of the second REE ions is always delayed relative to the first ions. The largest phase shifts are detected in Tb III and Th III lines. Pulsational variability of the Th III lines is detected here for the first time. The Y II lines deviate from this picture, showing even lower amplitudes than Eu II lines but half a period phase shift relative to other weakly pulsating lines. We measured an extra broadening, equivalent to a macroturbulent velocity from 4 to 11−12 km s^{-1} (where maximum values are observed for Tb III and Th III lines), for pulsating REE lines. The surface magnetic field strength is derived for the first time for three roAp stars: HD 9289 (2 kG), HD 12932 (1.7 kG), and HD 19918 (1.6 kG).

Conclusions. The roAp stars exhibit similarity in the depth-dependence of pulsation phase and amplitude, indicating similar chemical stratification and comparable vertical mode cross-sections. In general, pulsations waves are represented by a superposition of the running and standing wave components. In the atmospheres of roAp stars with the pulsation frequency below the acoustic cut-off frequency, pulsations have a standing-wave character in the deeper layers and behave like a running wave in the outer layers. Cooler roAp stars develop a running wave higher in the atmosphere. In stars with pulsation frequency close to the acoustic cut-off one, pulsation waves have a running character starting from deep layers. The transition from standing to running wave is accompanied by an increase in the turbulent broadening of spectral lines.

Key words. stars: atmospheres – stars: chemically peculiar – stars: magnetic fields – stars: oscillations

1. Introduction

About 10% to 20% of upper main sequence stars are characterised by remarkably rich line spectra, often containing numerous unidentified features. Compared to the solar case, overabundances of up to a few dex are often inferred for some iron-peak and rare-earth elements, whereas some other chemical elements are found to be underabundant (Ryabchikova et al. 2004). Some of these *chemically peculiar* (Ap) stars also exhibit organised magnetic fields with a typical strength of a few kG. Chemical peculiarities are believed to result from the influence of the magnetic field on the diffusing ions, possibly in combination with

the influence of a weak, magnetically-directed wind (e.g., Babel 1992).

More than 30 cool Ap stars exhibit high-overtone, low-degree, non-radial p-mode pulsations with periods in the range of 6−21 min (Kurtz & Martinez 2000), with their observed pulsation amplitudes modulated according to the visible magnetic field structure. These *rapidly oscillating Ap* (roAp) stars are key objects for asteroseismology, which presently is the most powerful tool for testing theories of stellar structure and evolution.

Recent progress in observational studies of roAp stars has been achieved by considering high time-resolution spectroscopy in addition to the classical high-speed photometric measurements. High-quality time-resolved measurements of magnetic pulsators have revealed a surprising diversity in the pulsational behaviour of different lines in the roAp spectra (e.g., Kanaan & Hatzes 1998; Kurtz et al. 2006, and references therein). Detailed analyses of the bright roAp star γ Equ (Savanov et al. 1999;

Kochukhov & Ryabchikova 2001a) demonstrate that spectroscopic pulsational variability is dominated by the lines of rare-earth ions, especially those of Pr and Nd, which are strong and numerous in the roAp spectra. On the other hand, light and iron-peak elements do not pulsate with amplitudes above $50-100$ m s^{-1}, which is at least an order of magnitude lower in comparison with the $1-5$ km s^{-1} variability observed in the lines of rare-earth elements (REE). Many other roAp stars were proven to show very similar overall pulsational behaviour (e.g., Kochukhov & Ryabchikova 2001b; Balona 2002; Mkrtichian et al. 2003; Kurtz et al. 2005a), with an exceptional case in 33 Lib, which shows small-amplitude variations in Fe lines, and possibly two other stars, HD 12932 and HD 19918, where RV variations in the Fe I 5434.52 Å line have been marginally detected (Kurtz et al. 2005b).

The early spectroscopic studies speculated that the unusual diversity of the pulsation signatures in roAp spectra can be attributed to an interplay between the *p*-mode pulsation geometry and inhomogeneous horizontal or vertical element distributions (see discussions in Kanaan & Hatzes 1998; Savanov et al. 1999; Baldry & Bedding 2000; Mkrtichian et al. 2000). However, none of these studies present models capable of explaining pulsations in real stars. Peculiar characteristics of the *p*-mode pulsations in a roAp star were finally clarified by Ryabchikova et al. (2002), who were the first to empirically determine vertical stratification of chemical elements and relate chemical profiles to pulsational variability. In their study of the atmospheric properties of γ Equ, Ryabchikova et al. show that the light and iron-peak elements are enhanced in the lower atmospheric layers, whereas REE ions are concentrated in a cloud with a lower boundary at $\log \tau_{5000} \lesssim -4$ (Mashonkina et al. 2005). Thus, high-amplitude pulsations observed in REE lines occur in the upper atmosphere, while lines of elements showing no significant variability form in the lower atmosphere. This leads to the following general picture of roAp pulsations: we observe a signature of a magnetoacoustic wave, propagating outwards through the chemically stratified atmosphere with increasing amplitude.

In addition to remarkable pulsational behaviour, the REE lines formed in the upper atmospheric layers of roAp stars exhibit an extra broadening, corresponding to a macroturbulent velocity $V_{\mathrm{macro}} = 10$ km s^{-1}, which cannot be attributed to the chemical stratification or magnetic field effects (Kochukhov & Ryabchikova 2001a). In the recent detailed line-profile variability study, Kochukhov et al. (2007) have presented evidence for the existence of peculiar asymmetric oscillation patterns in the broad REE lines of several roAp stars. It was demonstrated that the inferred pulsation signatures can be reproduced with the spectrum synthesis calculations, which contain an extra pulsational line width variability in addition to the usual velocity perturbations. These results suggest that a turbulence zone modulated by pulsations probably exists in the upper atmospheres of roAp stars.

The presence of significant phase shifts between pulsation radial velocity (RV) curves of different REEs (Kochukhov & Ryabchikova 2001a) or even lines of the same element (Mkrtichian et al. 2003) can be attributed to the chemical stratification effects and, possibly, to a short vertical length of running magnetoacoustic wave. However, it is not immediately clear whether all spectroscopic observations of roAp stars can be fitted into this simple picture and to what extent magnetoacoustic pulsation theories can explain these observations. The wide diversity of pulsation signatures (in particular, phases and bisector variability) of the REE lines probing similar atmospheric heights and, especially, the presence of pulsation node in the atmosphere

of 33 Lib (Mkrtichian et al. 2003) are inexplicable in the framework of the non-adiabatic pulsation models developed by Saio & Gautschy (2004) and Saio (2005). These calculations correctly predict an increase in pulsation amplitude with height, but show neither nodes nor rapid phase changes in the REE line-forming region. To resolve this discrepancy it is therefore imperative to analyse in detail pulsational variations of many different ions in the spectra of representative sample of roAp stars. Only in this way can we derive meaningful observational constraints for pulsation theories and search for regular patterns in the pulsation characteristics of different roAp stars.

First general results for roAp stars were presented by Kurtz et al. (2005a). They considered bisector behaviour of the Hα core and the Nd III 6145 Å line in 10 roAp stars. Based on the Hα core measurements, the authors point out that the increasing amplitude with height in the atmosphere is a common characteristic of all stars in their sample. Kurtz et al. (2005a) also note that in some stars, e.g. HD 12932, pulsations have a standing-wave behaviour, while more complex pulsations are observed in some other stars. These results were obtained from the analysis of bisector variability of one particular line, Nd III 6145 Å. This feature is not optimal for the bisector analysis because of the different blending effects both in the line core and the line wings that depend on the effective temperature and/or chemical anomalies.

In this study we have embarked on the task of obtaining a detailed vertical cross-section of the roAp pulsation modes. We used the unique properties of roAp stars, in particular chemical stratification, to resolve the vertical structure of *p*-modes and to study propagation of pulsation waves at a level of detail, that was previously only possible for the Sun. Our *pulsation tomography* approach consists of characterising the pulsational behaviour of a carefully chosen, but extensive, sample of spectral lines including weak ones and subsequently interpretating the observations in terms of pulsation wave propagation. Therefore, our sample was limited to slowly rotating roAp stars. The aim of this analysis is to derive observationally a complete picture of how the amplitude and phase of magnetoacoustic waves depend on depth and to correlate resulting vertical mode cross-sections with other pulsational characteristics and with the fundamental stellar parameters. Furthermore, we envisage that unique 3D maps of roAp atmospheres and non-radial pulsations can be derived by combining pulsation tomography results presented here with the horizontal pulsation maps obtained with Doppler imaging (Kochukhov 2004) or moment analysis (Kochukhov 2005).

Our paper is organised as follows. Section 2 describes acquisition and reduction of roAp time-series spectra. The choice of targets and physical properties of the stellar sample are discussed in Sect. 3. Radial velocity measurements and period analysis are presented in Sect. 4. Pulsation tomography results are summarised in Sect. 6. Bisector variability is analysed in Sect. 5. Results of our study are summarised and discussed in Sect. 7.

2. Observations and data reduction

The main observational dataset analysed in our study consists of 958 observations of 8 roAp stars, obtained with the UVES instrument at the ESO VLT between October 8, 2003 and March 12, 2004 in the context of the observing programme 072.D-0138 (Kurtz et al. 2006). The ESO Archive facility was used to search and retrieve science exposures and the respective calibration frames. Observations of each target covered 2 h and consisted of an uninterrupted high-resolution spectroscopic time-series with a total number of exposures ranging from 69

Table 1. Log of time-series observations for roAp stars.

Star	Start HJD (2 450 000+)	End HJD (2 450 000+)	Number of exposures	Exposure time (s)	Overhead time (s)	Peak S/N	Telescope/Instrument (observing mode)
HD 9289	2920.54506	2920.62881	111	40	25	90	VLT/UVES (600 nm)
HD 12932	2921.62234	2921.70532	69	80	25	90	VLT/UVES (600 nm)
HD 19918	2921.52607	2921.60905	69	80	25	100	VLT/UVES (600 nm)
HD 24712	3321.65732	3321.74421	92	50	22	300	VLT/UVES (390+580 nm)
HD 101065	3071.67758	3071.76032	111	40	25	180	VLT/UVES (600 nm)
HD 122970	3069.70977	3069.79359	111	40	25	160	VLT/UVES (600 nm)
HD 128898	3073.80059	3073.88262	265	1.5	25	250	VLT/UVES (600 nm)
HD 134214	3070.77571	3070.85848	111	40	25	260	VLT/UVES (600 nm)
HD 137949	3071.76312	3071.84598	111	40	25	350	VLT/UVES (600 nm)
HD 201601	2871.46470	2871.56295	70	80	42	80	SAO 6-m/NES (425–600 nm)
HD 201601	2186.70618	2186.80296	64	90	43	250	Gecko/CFHT (654–6660 nm)
HD 201601	2186.82456	2186.92308	65	90	43	230	Gecko/CFHT (662–673 nm)

to 265. The length of individual exposures was 40 s or 80 s, except for the brightest roAp star HD 128898 (α Cir), for which a 1.5 s exposure time was used. The ultra-fast (625 kHz/4pt) readout mode of the UVES CCDs allowed us to limit overhead to ≈ 20 s, thus giving a duty cycle of 70−80% for the majority of the targets. The signal-to-noise ratio (S/N) of individual spectra is between 90 and 350, as estimated from the dispersion of the stellar fluxes in the line-free regions. Detailed description of observations for each target is presented in Table 1. Columns of the table give the stellar name, heliocentric Julian dates for the beginning and the end of spectroscopic monitoring, number of observations, exposure and overhead times, peak signal-to-noise ratio of individual spectra, and information about the telescope and instrument where the data were obtained.

The red arm of the UVES spectrometer was configured to observe the spectral region 4960−6990 Å (central wavelength 6000 Å). The wavelength coverage is complete, except for a 100 Å gap centred at 6000 Å. Observations were obtained with the high-resolution UVES image slicer (slicer No. 3), providing an improved radial velocity stability and giving maximum resolving power for $\lambda/\Delta\lambda \approx 115\,000$.

All spectra were reduced and normalised to the continuum level with a routine especially developed by one of us (DL) for a fast reduction of spectroscopic time-series observations. A special modification of the Vienna automatic pipeline for échelle spectra processing (Tsymbal et al. 2003) was developed. All bias and flat field images were median-averaged before calibration. The scattered light was subtracted by using a 2D background approximation. For cleaning cosmic ray hits, we used an algorithm that compares the direct and reversed spectral profiles. To determine the boundaries of échelle orders, the code used a special template for each order position in each row across dispersion axes. The shift of the row spectra relative to template was derived by a cross-correlation technique. Wavelength calibration was based on a single ThAr exposure, recorded immediately after each stellar time series. Calibration was done by the usual 2D approximation of the dispersion surface. An internal accuracy of 30−40 m s^{-1} was achieved by using several hundred ThAr lines in all échelle orders. The final step of continuum normalisation and merging of the échelle order was carried out by transformation of the flat field blaze function to the response function in each order.

The global continuum normalisation was improved by iteratively fitting a smoothing spline function to the high points in the average spectrum of each roAp star. With this procedure we corrected an underestimate of the continuum level, unavoidable in analysis of small spectral regions of the crowded spectra of cool Ap stars. Correct determination of the absolute continuum level is important for retrieving unbiased amplitudes of radial velocity variability when the centre-of-gravity method is used. In addition to the global continuum correction, spectroscopic time series were post-processed to ensure homogeneity in the continuum normalization of individual spectra. Extracted spectra were divided by the mean, the resulting ratio was heavily smoothed, and then it was used to correct continua in individual spectra. Without this correction a spurious amplitude modulation of pulsation in variable spectral lines may arise due to an inconsistent continuum normalisation.

The red 600 nm UVES dataset was complemented by the observations of HD 24712 obtained on November 11, 2004 in the DDT program 274.D-5011. Ninety-two time-resolved spectra were acquired with the UVES spectrometer, configured to use the 390+580 nm dichroic mode (wavelength coverage 3300−4420 and 4790−6750 Å). A detailed description of the acquisition and reduction of these data is given by Ryabchikova et al. (2007).

For the roAp star HD 201601 (γ Equ), we analysed 70 spectra obtained on August 19, 2003 with the NES spectrograph attached to the 6-m telescope of the Russian Special Astrophysical Observatory. These échelle spectra cover the region 4250−6000 Å and have typical S/N of ≈ 80. The data were recorded by Kochukhov et al. (2004), who searched for rapid magnetic field variability in γ Equ. We refer readers to that paper for the details on the acquisition and reduction of the time-series observations at the SAO 6-m telescope.

Post-processing of the échelle spectra of HD 24712 and HD 201601 was done consistently with the procedure adopted for the main dataset. In addition, the time-resolved observations of HD 201601 obtained in 2001 using the single-order $f/4$ Gecko coudé spectrograph with the EEV1 CCD at the 3.6-m Canada-France-Hawaii telescope were used. Observations have a resolving power of about 115 000, determined from the widths of a number of ThAr comparison lines. The reduction is described in Kochukhov et al. (2007).

3. Fundamental parameters of programme stars

Fundamental parameters of the programme stars are given in Table 2. For six stars, effective temperatures $T_{\rm eff}$, surface gravity $\log g$, and mean surface magnetic fields $\langle B_{\rm s} \rangle$ were taken from the literature. For 4 remaining stars, HD 9289, HD 12932, HD 19918, and HD 134214, atmospheric parameters were derived using Strömgren photometric indices (Hauck & Mermilliod 1998) with the calibrations by

Table 2. Fundamental parameters of target stars.

HD number	Other name	T_{eff} (K)	$\log g$	$v_e \sin i$ (km s^{-1})	$\langle B_s \rangle$ (kG)	P (min)	Reference
9289	BW Cet	7840	4.15	10.5	2.0	*10.522*	this paper
12932	BN Cet	7620	4.15	3.5	1.7	*11.633*	this paper
19918	BT Hyi	8110	4.34	3.0	1.6	*11.052*	this paper
24712	DO Eri, HR 1217	7250	4.30	5.6	3.1	*6.125*, 6.282	Ryabchikova et al. (1997)
101065	Przybylski's star	6600	4.20	2.0	2.3	*12.171*	Cowley et al. (2000)
122970	PP Vir	6930	4.10	4.5	2.3	*11.187*	Ryabchikova et al. (2000)
128898	α Cir	7900	4.20	12.5	1.5	*6.802*, 7.34	Kupka et al. (1996)
134214	HI Lib	7315	4.45	2.0	3.1	*5.690*	this paper
137949	33 Lib	7550	4.30	$\leq$2.0	5.0	*8.271*,4.136, 9.422	Ryabchikova et al. (2004)
201601	γ Equ	7700	4.20	$\leq$1.0	4.1	*12.20*	Ryabchikova et al. (2002)

Moon & Dworetsky (1985) and by Napiwotzki et al. (1993) as implemented in the TEMPLOGG code (Rogers 1995). In addition Geneva photometric indices (Burki et al. 2005)[1] with the calibration of Künzli et al. (1997) was used for effective temperature determination. The colour excesses were estimated from the reddening maps by Lucke (1978). In Table 2 we present average values of the effective temperatures derived with three different calibrations. A typical dispersion is ±150 K.

In all stars but HD 101065, rotational velocities were estimated by fitting line profiles of the magnetically insensitive Fe I 5434.5, 5576.1 Å lines. Magnetic spectral synthesis code SYNTHMAG (Piskunov 1999; Kochukhov 2006a) was used in our calculations. Atomic parameters of spectral lines were extracted from the VALD (Kupka et al. 1999) and DREAM (Biémont et al. 1999) databases, supplemented with the new oscillator strengths for La II (Lawler et al. 2001), Nd II (Den Hartog et al. 2003), Nd III (Ryabchikova et al. 2006a), Sm II (Lawler et al. 2006), and Gd II (Den Hartog et al. 2006). We confirmed rotational velocities derived previously for HD 24712, HD 122970, HD 128898, HD 137949, and HD 201601. High spectral resolution of the present data allows us to improve the value of the projected rotational velocity for HD 101065 (Przybylski's star) using partially resolved Zeeman patterns in numerous lines of the rare-earth elements. The value of the magnetic field modulus, 2.3 kG (Cowley et al. 2000), was confirmed.

We note that the derived values of $v_e \sin i$ in very sharp-lined roAp stars depend strongly on the Fe stratification, which is known for some of them (e.g. γ Equ, see Ryabchikova et al. 2002) and is typically characterised by the Fe overabundance below $\log \tau_{5000} = -1$ and Fe depletion in the outer layers. Rotational velocities in Table 2 are derived for a homogeneous Fe distribution. However, in all programme stars we see observational evidence of Fe stratification, such as anomalous strength of the high-excitation lines compared to the low-excitation lines (see Ryabchikova et al. 2003). We tested one of the most peculiar stars, 33 Lib, for possible influence of stratification on the derived $v_e \sin i$ and found that including stratification may decrease the inferred rotational velocity to 1.5 km s^{-1} in comparison to 2.5–3.0 km s^{-1} obtained with a homogeneous Fe abundance distribution. The lower value of $v_e \sin i$ seems to fit the observed resolved and partially resolved Zeeman components better.

In three programme stars, HD 9289, HD 12932, and HD 19918, mean magnetic modulus was estimated for the first time from differential magnetic broadening/intensification. Two spectral regions with a pair of lines having different magnetic sensitivity were synthesised for a set of magnetic field strengths. The first region contain well-known Fe II 6147.7 Å ($g_{eff} = 0.83$)

and 6149.3 Å ($g_{eff} = 1.35$) lines, while Fe I 6335.3 Å ($g_{eff} = 1.16$) and 6336.8 Å ($g_{eff} = 2.00$) lines were analysed in the second spectral region. The derived values of the magnetic fields were confirmed by fitting other magnetically sensitive lines, for example, Fe II 6432.7 Å ($g_{eff} = 1.82$) and Eu II 6437.6 Å ($g_{eff} = 1.76$).

4. Radial velocity measurements

To perform a meaningful study of the pulsational amplitudes in spectral lines of different chemical elements/ions, one has to be very careful in the choice of lines for pulsation measurements. For this purpose we have synthesised the observed spectral region for each star with the model atmosphere parameters and magnetic field values from Table 2. Abundances for HD 24712, HD 101065, HD 122970, HD 128898, HD 137949, and HD 201601 were taken from the papers cited in the last column of Table 2. For the remaining four stars, a preliminary abundance estimate was obtained in this paper.

The radial velocities were measured with a centre-of-gravity technique. We used only unblended or minimally blended lines. In some cases where the line of interest was partially overlapping with the nearby lines, only the unblended central part of the line was considered; therefore, some lines were not measured between the continuum points. This usually leads to lower pulsation amplitudes if we have strong variations in the pulsation signal across a spectral line (see γ Equ – Sachkov et al. 2004; and HD 99563 – Elkin et al. 2005). Bisector radial velocity measurements were performed for Hα core and for a subset of Y II, Eu II, Nd II, Nd III, Pr II, Pr III, Tb III, and Th III spectral lines. The pulsational RV variability of the two strongest Th III lines at $\lambda\lambda$ 5376.13 and 6599.48 Å was investigated for several stars in our sample for the first time.

A detailed frequency analysis of the RV data for 8 stars from our sample was carried out by Kurtz et al. (2006). These authors used the same observations as we do and, despite the relatively short time span (2 h) of the spectroscopic time series, they claimed to resolve several frequencies for each star and to find amplitude modulation that was not observed in photometry. Although a detailed frequency analysis is not the primary goal of our paper, we did repeat time-series analysis for all lines. First we applied the standard discrete Fourier transformation (DFT) to the RV data. The period corresponding to the highest pulsation amplitude value was then improved by the sine-wave least-square fitting of the RV data with pulsation period, amplitude, and phase treated as free parameters. This fit was removed from the data and then Fourier analysis was applied to the residuals. This procedure was repeated for all frequencies with the S/N above 5.
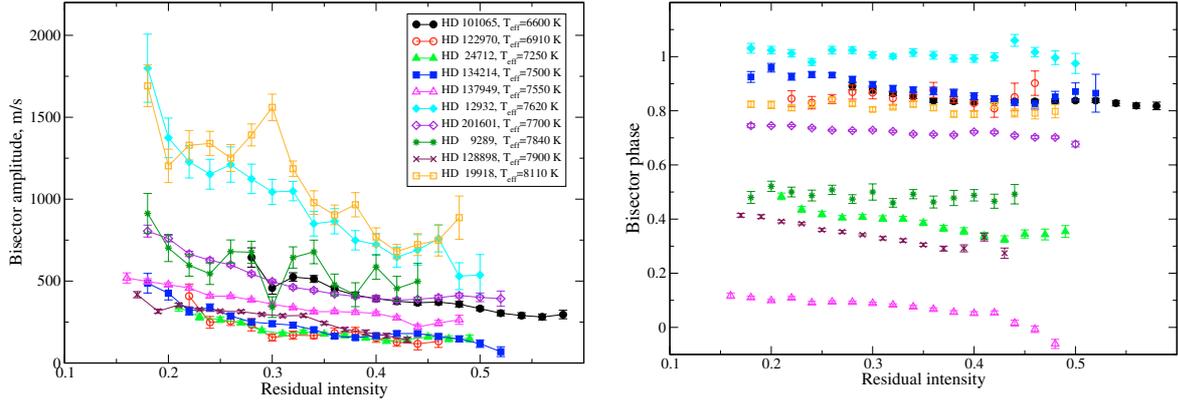
---

[1] http://obswww.unige.ch/gcpd/ph13.html

Fig. 1. Bisector measurements in the Hα core for the programme stars. The RV amplitudes are shown in *the left panel* and pulsation phases (based on the main periods from Table 2) in *the right panel*.

To verify our analysis against the results of Kurtz et al. (2006), we applied it to the set of Pr III lines (to each line separately and to the average Pr III RV) and compared in detail the resulting solution for HD 134214. Our frequency solution agrees perfectly with Kurtz et al. (2006), although our RV amplitudes are systematically lower. We believe that the primary reason for this discrepancy, which is present for other stars as well, is our systematically higher continuum placement, leading to lower pulsation amplitude when the centre-of-gravity method is used. As explained in Sect. 2, we have rectified observations with a spline-fit over wide wavelength regions, whereas Kurtz et al. (2006) have probably assigned continuum points to the high spectrum points in the immediate vicinity of the line considered.

For each spectral line, we estimated the probability that the detected periodicity is not due to noise (Horne & Baliunas 1986). Then, for the lines with probabilities higher than 0.999, we calculated a weighted average value of the pulsation period. All amplitudes and phases were then recalculated keeping the period fixed. This information is summarised in Table 3 (available online only) for all lines studied in each star. Table 3 contains amplitudes (first line) and phases (second line), together with the corresponding errors for the dominant pulsation period. When no pulsation signal was detected, we give the formal amplitude solution for the fixed period without phase information. If a star had one dominant period, the RV analysis was done with this period. In the cases of more than one dominant period, a simultaneous fit was performed with up to three periods. RV variation was approximated with the expression

$$\langle V \rangle = V_0(t - t_0) + \sum_{i=1}^{3} V_i \cos\{2\pi[(t - t_0)/P_i - \varphi_i]\}. \quad (1)$$

Here the first term takes possible drift of the spectrograph's zero point into account. For all stars but HD 24712, HJD of the first exposure of the star at a given night was chosen as a reference time t_0. For HD 24712, HJD = 2453320.0 was used as a reference time. Both V_i and φ_i are, respectively, amplitude and phase of the RV variability with the ith period ($i_{max} = 3$). With the minus sign in front of φ_i, a larger phase corresponds to a later time of RV maximum. This phase agreement is natural when discussing effects of the outward propagation of pulsation waves in the atmospheres of roAp stars.

The periods employed for determining of the RV amplitudes and phases are given in the seventh column of Table 2. When more than one period was inferred in the fitting procedure, the main period for which pulsation amplitudes and phases are given in Table 3 (online material) is highlighted with italics.

5. Bisector measurements

Radial velocity analysis was complemented by studying bisector variability. Figure 1 shows bisector amplitudes (left panel) and phases (right panel) across the core of Hα line calculated with the pulsation periods from Table 2. Where two periods or the main period and its first harmonic are resolved, simultaneous fit with two frequencies was done. In all programme stars, an increase in bisector amplitude by two or more times from the transition region to the deepest part of the core is observed. Thus we supported the conclusion made by Kurtz et al. (2005a). This change is gradual in all but two stars: HD 9289 and HD 19918, which have the lowest S/N. It is, therefore, unclear if small jumps of RV amplitude across the core are real or caused by the low S/N of the spectroscopic data. RV changes are accompanied by tiny phase changes. Only in four stars do phase changes exceed the error bars. These are the stars with the shortest pulsation periods close to the acoustic cut-off frequencies: HD 24712, HD 128898, HD 132214, and HD 137949 (33 Lib). The NLTE calculations show that, in the atmosphere of the star with T_{eff} between 7000 and 8000 K, the Hα core is formed at $-5 \lesssim \log \tau_{5000} \lesssim -2$ (Mashonkina, private communication). It is applied to a normal atmosphere; however, a core-wing anomaly is present in all programme stars (Cowley et al. 2000), which was attributed to a peculiar atmospheric stratification containing a region of increased temperature below $\log \tau_{5000} = -4$ (Kochukhov et al. 2002). This change in the atmospheric structure may lead to an upward shift in formation depth of the base of the Hα core (Mashonkina, private communication).

More care should be taken in the choice of metal spectral lines for the bisector measurements than for the centre-of-gravity RV analysis. Blends with non-pulsating lines change the run of bisector pulsation amplitude across the line profiles, while blends with pulsating lines (weak REE lines in far wings, for example) may change both amplitudes and phases. These artifacts often lead to the wrong conclusion about roAp pulsational behaviour, especially when these conclusions are based on analysis of only one line. For instance, the well-known Nd III 6145.068 Å line, analysed in many pulsation studies, is blended with the Si I 6145.016 Å line and with the Ce II 6144.853 Å. The latter feature makes a non-negligible contribution to the spectrum of Przybylski's star. The strongest Nd III 5294.11 Å line is blended
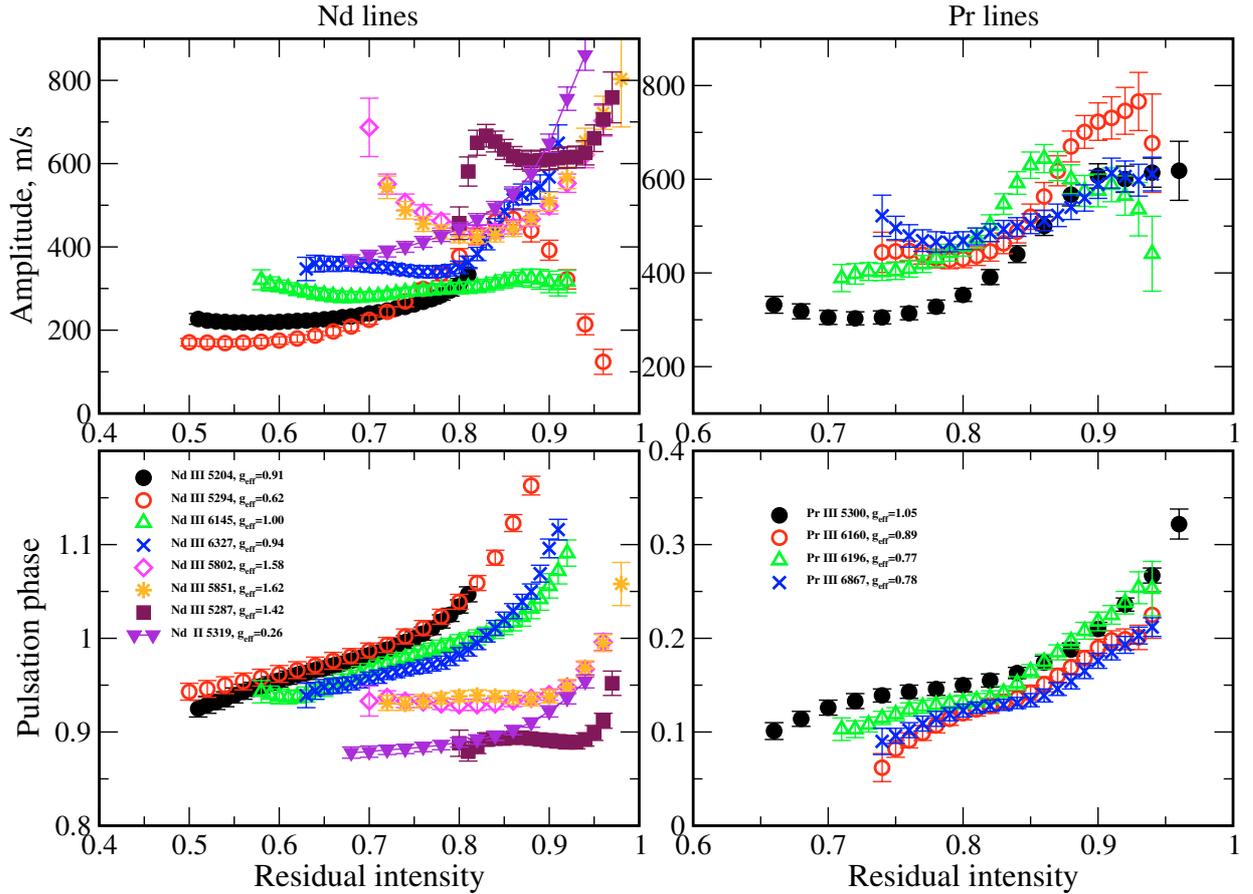
Fig. 2. Bisector measurements as a function of the Nd (*left panels*) and Pr (*right panels*) lines' residual intensity in HD 134214. *Top panels* represent RV amplitudes, and *bottom panels* show pulsation phases calculated with the main period from Table 2.

with the Fe I 5293.96 Å line in the blue wing and with the high-excitation Mn II 5294.32 Å line in the red wing. Both lines are normally weak, but they are strengthened in the stratified atmospheres of roAp stars with the effective temperatures higher than 7000−7200 K. This blending results in a drop of the bisector velocity amplitudes starting from some intensity points in the line profile. Zeeman splitting may also change velocity amplitude distribution across the line profile. Figure 2 illustrates the influence of blends and Zeeman effect on the bisector amplitudes and phases of Nd II- III and Pr III lines in HD 134214. Pairs of Nd III lines with similar intensities and Zeeman structure have identical bisector phases independent of any blending. Thus, phases may be considered as a more reliable indicator of the pulsational characteristics. One may see that, up to the residual intensity 0.85, the Nd III 5294 Å line shows the same bisector velocity amplitudes as another strong Nd III line at 5204 Å. However, after this intensity point, the two amplitude curves start to deviate: in the Nd III 5294 Å line, the amplitude drops towards the line wings, probably due to blends. Also blends decrease bisector amplitudes in the Nd III 6145 Å compared to the Nd III 6327 Å line, which has the same intensity and Zeeman structure. Three out of the four Pr III lines shown in Fig. 2 are practically free of blends in most of the programme stars, and additionally, these lines have identical Zeeman splitting, which results in similar bisector pulsational behaviour.

As shown in Sect. 6, Tb III lines exhibit a particularly interesting pulsation behaviour, so their blending should be investigated in detail. The Tb III lines are not as strong and numerous as Pr III and Nd III. From 10 lines only the strongest one, Tb III 5505 and three others, 5847, 6323, and 6687 Å, may be used for bisector measurements. Most often we measured the Tb III 5505.408 Å line. This line is blended by the Ce II 5505.204 Å in the blue wing and by Ce II 5505.588 Å in the red wing. The Tb III λ 6323.619 Å line is free of blends but may be partially blended with the weak atmospheric O_2 line at λ 6323.75 Å. Figure 3 shows a spectral region around the Tb III 5505.408 Å line in HD 101065, where the blending problem is the most severe. For comparison we show the region with the Tb III 6323.619 Å line; therefore, wavelength scale is given in km s^{-1} relative to the centre of each line. We also show synthetic spectrum calculated with the highest possible Ce abundance and magnetic field strength appropriate for HD 101065 (see Table 2). Although the full intensity of the calculted feature is equal to the intensity of the observed one, for demonstration of the blending effects we did not convolve synthetic spectrum with the instrumental and rotational profiles. Note that the red wing of the Tb III 6323.619 Å line is blended with the atmospheric O_2 line 6323.75, therefore no bisector measurements were carried out above intensity level 0.9. The blue wing asymmetry in both Tb III lines is rather an effect of the hyperfine splitting, than the real influence of blends, because the same asymmetry is observed in other stars where the Ce II contribution is negligible.

Taking into account the similarity of the RV amplitudes and, in particular, phases in the bisector measurements of both lines
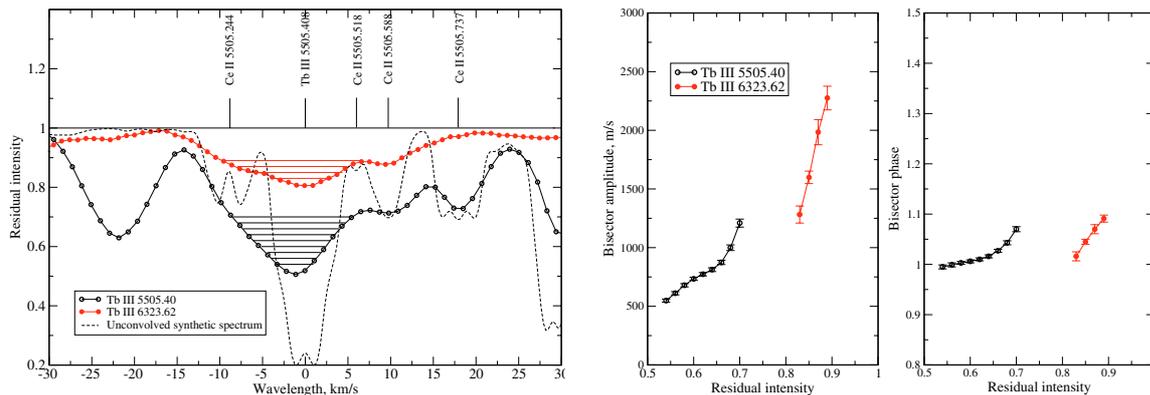
Fig. 3. Tb III lines in HD 101065. *Left panel* represents the observed and calculated line profiles, and the *two next panels* show the RV amplitudes and pulsation phases determined for the intensity levels indicated in the corresponding line profiles by the horizontal lines.

we conclude that even in HD 101065 the blending does not affect seriously the measured pulsation characteristics.

6. Phase-amplitude diagrams

Empirical understanding and detailed theoretical interpretation of the pulsation phenomenon in roAp stars requires construction of the vertical cross-section of pulsation modes. Chemical stratification enables this difficult task by separating formation layers of the spectral lines of different chemical elements far apart, thus allowing us to resolve the vertical dimension of pulsating Ap-star atmospheres, as can be done for no other type of pulsating stars. However, the key information needed for such vertical pulsation tomography – formation depth of REE spectral lines – is difficult to obtain. Early studies (e.g., Kanaan & Hatzes 1998) have suggested that the line intensity may be used as a proxy of the relative formation heights. However, it is now understood that the chemical stratification effects are dominant in the atmospheres of cool Ap stars and, therefore, formation region of weak lines of one element is not necessarily located deeper than the layer from where the strong lines of another element originate. This is why a comparison of the intensities of different pulsating lines is only meaningful for the absorption features of the same element/ion.

The study by Ryabchikova et al. (2002) presented the first comprehensive analysis of the vertical stratification of light, iron-peak, and rare-earth elements in a roAp star, demonstrating that only by taking height-dependent abundance profiles into account can one calculate correct formation depths of pulsating spectral lines and meaningfully interpret the results of time-resolved spectroscopy. In a later paper, Mkrtichian et al. (2003) study the vertical profiles for *p*-mode oscillations in 33 Lib (HD 137949) using pulsation centre-of-gravity measurements for individual lines. To establish the vertical atmospheric coordinate, the authors used the $W_\lambda - \log\tau$ transformation scale in 33 Lib's atmosphere by assuming homogeneous elemental distribution. This simplified approach was sufficient for detecting the node in the Nd II, Nd III line-forming region – a discovery later confirmed by Kurtz et al. (2005b) and by the present paper. However, as Mkrtichian et al. (2003) themselves acknowledge, their method is too simplified because it ignores the vertical and horizontal inhomogeneous distribution of chemical abundances. Indeed, their technique cannot be used for simultaneous interpretation of the pulsational variability of different elements since Fe, as well as Ca, Cr and all REE elements, are strongly stratified in the atmosphere of 33 Lib and other roAp stars (see

Ryabchikova et al. 2004), and stratification is not the same for different elements. Mkrtichian et al. (2003) suggest that in future studies some of these difficulties can be alleviated by the "multi-frequency tomographic approach" that will use the phase and amplitude profiles of different oscillations modes to establish a link to the atmospheric geometric depth scale.

In general, the detailed pulsation tomography analysis of roAp stars should be based on sophisticated atmospheric modelling including chemical stratification, NLTE, magnetic field, and eventually, pulsation effects on the shape and intensity of spectral lines with substantial RV variability. Such modelling is very demanding in terms of the quality of observations, required input data, and computer resources. This is why only two roAp stars, γ Equ and HD 24712, have been studied with this method up to now (Mashonkina et al. 2005; Ryabchikova et al. 2006b). Here we suggest a different approach to the pulsation tomography problem. In the framework of the outward propagating magnetoacoustic wave, one expects a continuous amplitude versus phase relation for pulsation modes. Lines showing later RV maximum should originate higher in the atmosphere. Thus, new insight into the roAp pulsation modes structure can be obtained by inferring and interpreting the trend in pulsation velocity amplitude as a function of pulsation phase. Such phase-amplitude diagrams offer a possibility of tracing the vertical variation in the mode structure without tedious assignment of the physical depth to each pulsation measurement.

We note that this paper is not the first one to use the phase-amplitude diagrams for roAp stars. Baldry et al. (1998) and Baldry & Bedding (2000) produced similar diagrams in the pulsational studies of α Cir and HR 3831. However, their diagrams described pulsational properties not for individual lines with a proper identification but for small spectral regions often containing several spectral lines, sometimes without correct identification. As a result, the most important information on wave propagation was lost (see Sect. 6.5).

For each programme star we have produced phase-amplitude diagrams using a set of lines of representative chemical species, including Y II, Eu II, the Hα core, La II, Dy II, Dy III, Nd II, Nd III, Pr II, Pr III, Tb III, and Th III. We considered velocity amplitudes and phases derived with both the centre-of-gravity RV measurements and the bisector analysis. The line blending varies significantly from star to star due to different effective temperatures and chemical anomalies, therefore we cannot use identical set of spectral lines for all stars. For each star we tried to employ unblended or minimally blended lines, in particular, for the bisector measurements. In addition, the line broadening expressed
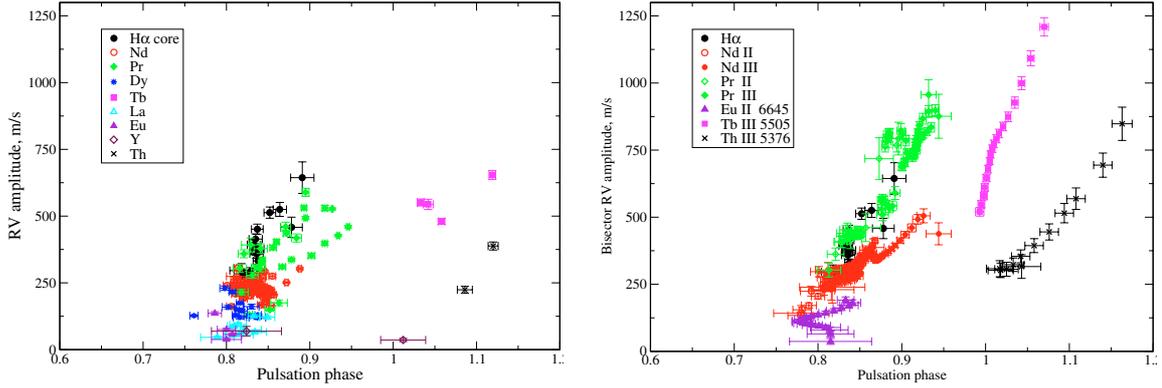
Fig. 4. Amplitude-phase diagrams for the pulsation centre-of-gravity measurements (*left panel*) and bisector measurements (*right panel*) in HD 101065.

in the terms of macroturbulent velocity was estimated for a few representative lines of each chemical species. This information is useful for assessing the isotropic velocity component at the formation heights of REE lines.

Below we present the results for individual stars.

6.1. HD 101065 (Przybylski's star)

The atmosphere of HD 101065 is known to be very rich in REE and underabundant in most other elements, including the Fe-peak species. Due to the low effective temperature, slow rotation, and abundance anomalies, most lines in the spectrum of HD 101065 are strong and sharp. As a result, one can achieve impressive accuracy of pulsation measurements, typically $\sim$5–8 m s^{-1}, for moderately strong lines. Although it is not easy to find unblended Fe lines in the forest of the REE lines, we managed to measure a few of them and to detect no pulsational variability above 30 m s^{-1}. Pulsation amplitudes at the level of 6 to 17 m s^{-1} were detected in the cores of very strong Ba II $\lambda\lambda$ 6142, 6496 Å lines, which gives us an idea about pulsation amplitudes close to the photospheric layers.

The centre-of-gravity and bisector phase-amplitude diagrams for HD 101065 are shown in Fig. 4. The centre-of-gravity measurements give us a general idea of the pulsation wave propagation in roAp atmosphere. Pulsations are characterised by the amplitude $\sim$40 m s^{-1} at the levels of the Y II, La II, and strong Eu II line formation. Then they pass, with the gradually increasing amplitude, the layers where the Dy II, Dy III, Nd II, Pr II, Nd III, the Hα core and Pr III lines are formed. The phase does not change by more than 0.15 of the pulsation period (less than 1 radian) from Eu II to Pr III lines. After that, a rapid change in pulsation phase occurs in Tb III and, next, in Th III lines. We measured two unblended Th III lines at λ 5376.13 and 6599.48 Å.

HD 101065 is the only star in our sample that shows similar pulsation signatures (bisector amplitude versus pulsation phase) for the Hα core, Nd II, Nd III, Pr II and weak Pr III lines. For all these features we find an increase in both pulsation amplitude and phase from the line wings to the line core. Kurtz et al. (2005a) have obtained similar amplitudes and phases for the Hα core and, based on the bisector measurements of the single Nd III 6145 Å line, they argue that the formation layers of Nd III lines start above the layers of formation of the deepest part of the Hα core. Our Fig. 4 provides strong evidence that most of REE lines, including Pr II and weaker Pr III lines, are formed in the same layers as the Hα core.

In addition we analysed the broadening of pulsating lines. All low-amplitude Ce II lines do not exhibit any extra broadening above the adopted value of the projected rotation velocity. All Eu II lines and Dy and Nd lines in both ionisation states show an extra broadening corresponding to V_{macro} between 2.5 and 4 km s^{-1}. Macroturbulent velocity grows from 5 km s^{-1} in weak Pr III 5765 Å line to 7–8 km s^{-1} in the strong Pr III lines $\lambda\lambda$ 5300, 6707 Å. We need $V_{\text{macro}} = 10$ km s^{-1} to fit the observed profiles of the unblended Tb III 6832 Å and Th III 5376 Å lines. It is worth noting that this rapid increase in the line broadening accompanies the change in the line profile variability pattern from the normal symmetric shape to the blue-to-red running waves, which become noticeable for the strongest Pr III lines and, in particular, for Tb III lines (Kochukhov et al. 2007). An extra broadening of the Pr III lines cannot be attributed to hyperfine structure.

Considering the amplitude-phase diagrams, we see a change in the pulsation behaviour for Tb III lines and, even stronger, for the Th III 5376.13 Å line. In contrast to the variability of the Hα core and Nd lines, we observe a rapid increase in the amplitude and in the phase from the line core to line wings in the lines of Tb III and Th III (see Fig. 5 – online only). This phenomenon cannot be explained by the pulsation wave propagating outwards.

In general, over the large fraction of the Przybylski's star atmosphere, up to the layers of the Nd III and weak Pr III line formation, pulsations are represented well by non-radial non-adiabatic p-modes (Saio 2005) with an amplitude increasing outward. Above these layers, pulsation characteristics change in a way that is not forseen by the theoretical models.

6.2. HD 122970

Pulsational observations of this star were obtained at the rotational phase 0.75, between the maximum and minimum of the magnetic field (see Fig. 3 in Ryabchikova et al. 2005a). The centre-of-gravity and bisector phase-amplitude diagrams for HD 122970 are presented in Fig. 6 (online only). For a few chosen lines we also show the variability of the pulsational characteristics along the line profiles in Fig. 7.

The overall pulsational behaviour in the atmosphere of this star is similar to HD 101065: low-amplitude pulsations are seen in Y II and Eu II lines, the amplitude increases slightly in the layers where the Hα core forms, and then it increases further in the Dy and Nd line formation layers. A rapid growth of the amplitude occurs in the region of the Pr line formation. Up to these
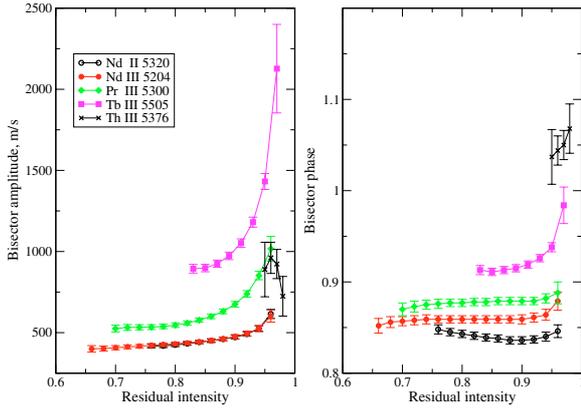
Fig. 7. Bisector measurements as a function of lines residual intensity in HD 122970. *The left panel* represents RV amplitudes, *right panel* shows pulsation phases calculated with the main period from Table 2.

layers, pulsations have a standing-wave character, with almost constant phases for all lines of Y II, Eu II, La II, Dy, Nd, and Pr. The phase shifts become noticeable for Tb III and Th III lines, as in HD 101065, and, again, in these lines pulsation amplitude and phase increase from the line core to line wing, contrary to predicted effect of the outward-running wave. While in HD 101065 the regions of the Hα core, Nd, and Pr line formation are the same or, at least, partially overlap, in HD 122970 the phase-amplitude diagrams show a significantly more stratified atmospheric structure.

Ryabchikova et al. (2000) noted that the projected rotational velocities derived from the REE lines are lower than those obtained from Fe-peak lines. More precise present observations confirm this result. We determined $v_e \sin i \approx 3.5$ km s^{-1} from the REE line fitting, whereas the Fe-peak elements show broadening corresponding to $v_e \sin i = 4.5$ km s^{-1}. A 3.877 d rotation period obtained by Ryabchikova et al. (2005a) for HD 122970, together with the low $v_e \sin i$, suggests a nearly pole-on geometry. Therefore, the difference in the apparent rotational velocities of the Fe-peak and REE lines may indicate a concentration of the REEs near the visible stellar rotation pole. No extra broadening is required to fit the Nd II, Nd III, Pr II, and weak Pr III lines, while $V_{macro} = 2-3$ km s^{-1} and 6 km s^{-1} are needed to fit the strong Pr III lines and the Th III 5376 Å line, respectively. The Y II lines, which show the smallest detectable RV amplitudes, have the same pulsation phases and extra broadening as strong Pr III lines.

The lines of the elements with $Z \leq 38$ do not show any pulsation amplitude above $7-20$ m s^{-1}. Two measured Zr II lines have amplitudes of ≈ 200 m s^{-1}.

6.3. HD 24712

According to the ephemeris given by Ryabchikova et al. (2005a), our pulsational observations were obtained at the rotational phase 0.944, i.e. close to the magnetic maximum. Detailed observational analysis of the spectroscopic pulsation signatures in HD 24712 was recently presented by Ryabchikova et al. (2007). HD 24712 is the only roAp star for which NLTE line formation calculations of Hα, Pr, and Nd were carried out (Mashonkina et al. 2005; Ryabchikova et al. 2006b). The observed intensities of the Nd and Pr lines in the first and the second ionisation states are explained by the stratified atmosphere with a step-like enhancement of these elements just above the NLTE

formation depth of the Hα core ($\log \tau_{5000} = -4$). Up to this atmospheric level, the observed distribution of pulsation phases agrees rather well with the predictions of the non-adiabatic pulsation models (see Fig. 1 in Kochukhov 2006b; and Fig. 3 in Sachkov et al. 2006), which is supported by the amplitude-phase diagrams for HD 24712 shown in Fig. 8 (online only). In contrast to the standing-wave dominated behaviour of HD 101065 and HD 122970, we see a running wave in HD 24712 from the low atmosphere, where the first pulsation signal is detected. Due to the availability of the simultaneous spectroscopic and photometric monitoring, the sequence of the pulsation phase changes is established with high accuracy in this star (Ryabchikova et al. 2007). Pulsation follows the same order as in HD 101065 and in HD 122970: Eu, La, Hα core, Nd, Pr, Tb lines.

The phase distribution with the optical depth, as well as our amplitude-phase diagrams, shows the phase shifts between Hα and Nd lines and between Pr and Nd lines. The NLTE calculations do not predict a significant difference in the location of the Pr and Nd line formation regions, therefore the observed phase shift is probably caused not by the vertical distribution of chemical elements, but by the horizontal abundance inhomogeneities. According to the pulsation phases, Nd lines have to be formed at the same layers as the deeper parts of the Hα core. At the same time, we caution that the existing NLTE calculations of Hα, Pr, and Nd lines are very preliminary, and they do not include potentially important effects of stratified abundance distribution on the atmospheric structure and neglect an influence of the magnetic desaturation on the line formation.

The bisector velocity amplitudes of HD 24712 are either constant along the line profile, or they slightly increase from the line wings to the line core, except for the Tb III and, possibly, Y II lines, in which bisector amplitude increases from the line core to the line wings (Fig. 9 – online only). Pulsation phases are nearly constant along the profiles of most lines, but show a tendency to grow from the line centre to the line wings for the strongest Pr III lines and for Tb III lines. Both Th III lines show pulsational amplitudes close to the detection limit. A very interesting result is obtained for Y II lines. Yttrium is the only element with $Z \leq 40$ whose lines have a measurable pulsation amplitude in HD 24712 (see Ryabchikova et al. 2007). These lines are strong enough to provide precise centre-of-gravity and bisector measurements, therefore pulsation phases can be determined with high accuracy. While RV amplitudes do not exceed $50-100$ m s^{-1} for the strongest Y II 5087 Å line, the bisector phase distribution across the line profile coincides with the phase distribution across the profile of the strongest Pr III 5300 Å line, which has an RV amplitude above 300 m s^{-1}. The estimated depth of formation of Y II lines in chemically homogeneous atmosphere lies around $\log \tau_{5000} = -1.5$ to -2.5, where the core of Hα line starts forming. Note that Doppler imaging of HD 24712 shows a similarity between yttrium and REE surface distributions (Lüftinger et al. 2006). The observed phase difference between Y II and the Hα and the coincidence of the phases in Y II and strong Pr III lines, on the one hand, and the large difference in amplitudes, on the other, is difficult to explain. We will see that the same pulsational behaviour of Y II lines is observed for some other roAp stars.

Although the projected rotational velocity of HD 24712 is rather high, spectral synthesis clearly shows that we need an extra broadening, equivalent to $V_{macro} = 6$ km s^{-1}, to fit strong Pr III lines, as well as Tb III and Th III lines, whereas no extra broadening is required for Nd lines. Interestingly, one needs $V_{macro} = 4$ km s^{-1} to reproduce the profile of the Y II 5087 Å line.
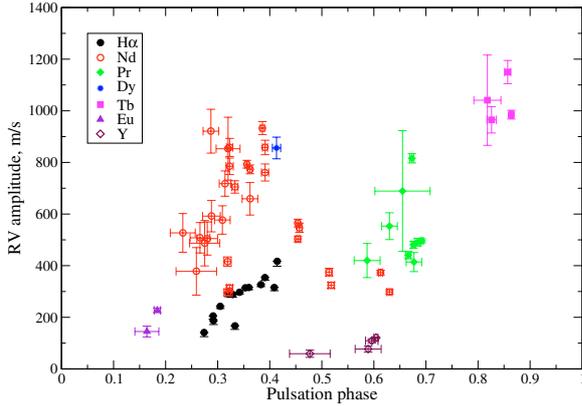
Fig. 11. Amplitude-phase diagrams for the pulsation centre-of-gravity measurements in α Cir.

Fig. 14. A comparison of the line profiles of different elements in HD 12932. Line profiles are scaled to the same central depth.

6.4. HD 134214

This star has one of the shortest pulsation periods, 5.7 min, which is close to the acoustic cut-off frequency calculated for HD 134214 by Audard et al. (1998). The centre-of-gravity and bisector amplitude-phase diagrams are shown for HD 134214 in Fig. 10 (online only). The amplitude-phase diagrams for this star are similar to those for HD 24712. In both stars we observe the running wave from the regions of Eu II line formation to Tb III, Th III line-forming regions. In HD 134214, all lines pulsating with high amplitude show an increase both in amplitude and in phase from the line core to the line wings (see Fig. 2).

The low rotational velocity allows us to partially resolve components of the Zeeman split lines, which makes the line profile analysis easier and, in particular, allows us to estimate an extra broadening accurately. An extra broadening of ~ 1 km s^{-1} is needed to fit the low-amplitude pulsating lines of Eu II. Then the inferred V_{macro} increases gradually: 4 km s^{-1} (Nd II, Dy III), 5−6 km s^{-1} (Nd III), 8−10 km s^{-1} (Pr III), 10 km s^{-1} (Tb III), and more than 10 km s^{-1} (Th III). Just as in HD 24712, Y II lines have small detectable RV amplitudes, but the same bisector phases as strong Pr III lines do. We measured $V_{\mathrm{macro}} \sim 6$ km s^{-1} for the Y II 5087 Å line.

In both stars the bisector amplitude-phase diagrams for Nd II and weaker Nd III lines are overlapping, which supports the model of the Nd stratification in roAp atmospheres proposed by Mashonkina et al. (2005). According to this model the strongest lines of Nd II are formed at the same layers as weak Nd III lines, therefore their pulsational characteristics should be similar.

No definite pulsation signatures are detected in the lines with $Z \leq 38$ and also in Zr II and Ba II lines. The upper RV amplitude limit is 10 m s^{-1}.

6.5. HD 128898 (α Cir)

The main photometric period of α Cir, one of the short-period roAp stars, is 6.83 min, which is close to the acoustic cut-off frequency. The amplitude-phase diagram for HD 128898 (Fig. 11) appears to be similar to those constructed for HD 24712 and HD 134214 and indicates a running wave. Based on an amplitude-phase diagram made for short spectral regions containing groups of unresolved lines, Baldry et al. (1998) suggested a high-overtone standing wave with a velocity node in the atmosphere of α Cir. This contradicts our results obtained from analysis of pulsations in isolated lines. Again, similar to HD 24712 and HD 134214, Y II lines have the smallest
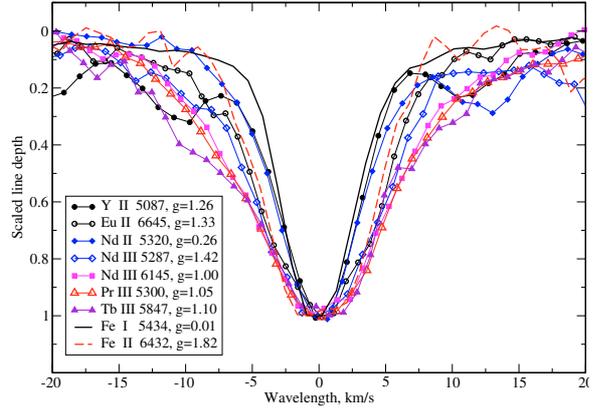
RV amplitudes, but the same phases as the strongest Nd III and Pr III lines.

The bisector analysis shows that bisector amplitude rapidly decreases from the line centre to the line wings with small changes in phase. This behaviour may be explained by a combination of non-radial pulsations and surface chemical inhomogeneity, which clearly manifests itself in the rotational modulation of the line profiles in α Cir (Kochukhov & Ryabchikova 2001b). The average spectrum used in the present study corresponds to the rotation phase 0.44 (minimum of the photometric pulsational amplitude) if we apply the ephemeris from Kurtz et al. (1994). All REE lines in our α Cir spectrum exhibit two-component profiles, which represents another proof of chemical spots.

6.6. HD 12932

Kurtz et al. (2006) suggest that HD 12932 is an example of the star with a standing wave behaviour in the layers of the Hα core formation based on the constancy of the bisector pulsation phases. Our measurements are presented in Fig. 12 (online only). While for Nd II and the Hα core the bisector phases are almost constant for a given line, the phases differ from line to line. Phase shifts are small, but reliable, taking the high accuracy of the phase determination into account (Fig. 13 – online only). The bisector phase measurements show that, if we attribute a given phase to the particular atmospheric height, many Nd lines should originate in extremely thin separate layers, which is impossible to explain.

Due to the slow rotation and a rather weak magnetic field, HD 12932 is useful for demonstrating the effect of differential extra broadening of the pulsating lines. Figure 14 presents a comparison between the line profiles of different elements/ions, scaled to the same central line depth. The wavelength scale is given in km s^{-1}, with line centre at zero velocity. The two iron lines with zero and large Zeeman broadening are shown to assess the expected magnetic field broadening effect. These lines, Fe I 5434 Å and Fe II 6432 Å, do not require any additional broadening other than Zeeman, instrumental, and rotational ones to fit the observed line profiles. The Eu II line broadening is explained by the combined Zeeman and hyperfine splitting. Our spectral synthesis shows a growth in the V_{macro} from Nd II lines (3−5 km s^{-1}), to Nd III lines (6−9 km s^{-1}), Pr III lines (7−10 km s^{-1}), and finally, to Tb III lines (10−11 km s^{-1}). The stronger line of the same ion, the larger V_{macro} is required to

fit the line profile. The Th III lines in HD 12932 are too weak for reliable measurements. The Y II 5087 Å line exhibits an extra broadening similar to Nd II lines, although no definite pulsation signal was detected in all measured Y II lines, as well as in the lines of Na, Mg, Si, Ca, Sc, Cr, Fe, Co, Ni, and Sr. No variability is detected in the Fe I 5434 Å line (RV amplitude 7 ± 15 m s^{-1}). Thus, we do not confirm results by Kurtz et al. (2005a), who claim a 3σ detection of pulsations in this line. We looked at 47 other lines of Fe I and Fe II, and we detected a pulsation signal exceeding the 3σ significance level only in seven features. For most of these lines weak variability is explained by blending with weak REE lines. Three out of six measured Ti II lines show a pulsation signal with the RV amplitudes $80-100$ m s^{-1}, while two T I lines did not reveal any variability. All three Ba II lines show RV amplitudes of ≈ 200 m s^{-1}.

6.7. HD 201601 (γ Equ)

The amplitude-phase diagrams for the centre-of-gravity measurements in γ Equ are shown in Fig. 15 (online only; left panel). Rather low spectral resolution of the γ Equ observations used for this type of pulsation measurements does not allow us to make a precise bisector study. For the bisector analysis we used the time-series observations of γ Equ carried out with the Gecko spectrograph at CFHT (see Kochukhov et al. 2007). The bisector amplitude-phase diagrams are displayed in Fig. 15 (right panel). If in the previous star, HD 12932, the RV amplitude remained nearly constant above a certain atmospheric height, in γ Equ we observed a continuous decrease of RV amplitude outward. The bisector amplitude-phase diagrams are fairly similar in both stars, showing the same constancy in the phase measured across Nd spectral lines and a phase shift between lines (Fig. 16 – online only). This phase shift is larger in γ Equ. Again, Y II lines have very small RV amplitudes, but their pulsation phases are the same as in the strongest Nd III and Pr III lines. Extra broadening of the REE lines in γ Equ was discussed by Kochukhov & Ryabchikova (2001a), who showed that $V_{\mathrm{macro}} = 10$ km s^{-1} is needed for fitting strong Nd III and Pr III lines.

6.8. HD 19918

Pulsational characteristics of HD 19918 (Fig. 18) are similar to both HD 12932 and, in particular, to γ Equ. An even more rapid decrease in the RV amplitude is observed in the atmosphere above a certain layer. The three stars show the largest RV amplitudes and the largest variation in the bisector velocity amplitudes from the line centre to the line wings (Fig. 17 – online only). In all these stars we find first an increase in the RV amplitudes with approximately constant phases (standing wave), and after that the pulsation wave transforms into a running one.

As in HD 12932, differential extra broadening is required to fit line profiles: $V_{\mathrm{macro}} = 0$ km s^{-1} (Fe), $V_{\mathrm{macro}} = 2-3$ km s^{-1} (Y II), $V_{\mathrm{macro}} = 4$ km s^{-1} (Eu II), $V_{\mathrm{macro}} = 7-8$ km s^{-1} (Nd II), $V_{\mathrm{macro}} = 8-10$ km s^{-1} (Nd III and Pr III), and $V_{\mathrm{macro}} = 11$ km s^{-1} (Tb III). Note that a smaller broadening is necessary to fit the line core than the line wings. Most line profiles show a triangular shape.

Kurtz et al. (2005a) report a detection of weak RV oscillations in the Fe I 5434 Å line. Our measurements confirm this result and also provide the following pulsation RV amplitudes for light and iron-peak elements: $30-50$ m s^{-1} for Na, Ca, Cr, Fe lines; ≈ 100 m s^{-1} for Ba II lines; $150-200$ m s^{-1} for Ti II lines.
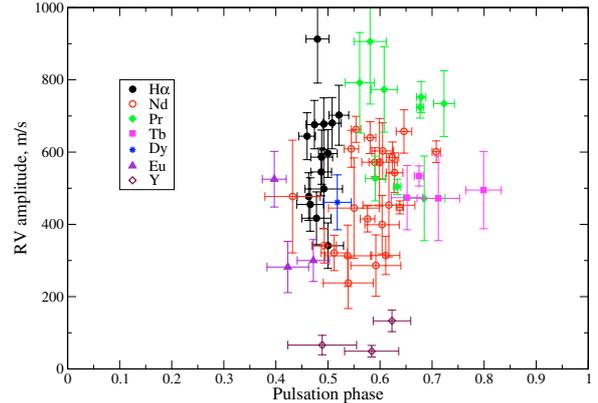
Fig. 19. The same as in Fig. 11 but for HD 9289.

6.9. HD 9289

The amplitude-phase diagrams for the centre-of-gravity measurements in the spectrum of HD 9289 are shown in Fig. 19. Because of the low S/N and significant rotation compared to other stars, we did not perform bisector measurements. The amplitude-phase diagrams for this star are similar to those for HD 12932.

6.10. HD 137949 (33 Lib)

33 Lib shows the most complex pulsational behaviour among all roAp stars. Mkrtichian et al. (2003) find nearly anti-phase pulsations of Nd II and Nd III lines, which they attribute to the presence of pulsation node high in the atmosphere of 33 Lib. This was confirmed by Kurtz et al. (2005b), who also find that in some REE lines the main frequency, corresponding to 8.27 min, and its harmonic have almost equal RV amplitudes. The high accuracy of the present observations allows us to study pulsational characteristics of the 33 Lib atmosphere in more detail. Figure 20 shows RV amplitudes (top) and phases (bottom) measured for the main period as a function of the central intensity of spectral lines. The NLTE Nd stratification analysis by Mashonkina et al. (2005) for HD 24712 shows that central intensities of both Nd II and Nd III lines are roughly proportional to there centre-of-gravity depth formation. Taking into account that the REE anomaly on which Nd stratification was based is the common feature for all roAp stars (Ryabchikova et al. 2001, 2004), we can expect similar REE gradients in the atmosphere of 33 Lib, hence, the similar dependence of the central intensities on the optical depth.

The phase jump is defined very well by Nd lines and is also indicated by the measurements of Pr, Tb, Dy lines. Our results show that the phase jump (radial node) does not separate the formation regions of the lines in consecutive ionisation states as is claimed by Kurtz et al. (2005b). Nd III, Pr III, and Th III lines are observed from both sides of the jump. Moreover, a position of the phase jump relative to line depth provides some evidence that abundance distributions for at least Pr, Nd, Tb, Dy are similar, hence one may expect abundance jumps at approximately the same optical depths in 33 Lib atmosphere.

Bisector measurements support the results obtained for the main frequency from centre-of-gravity measurements and allow us to carry out a more detailed study of the pulsation properties in 33 Lib. Figure 21 shows bisector amplitudes (top) and phases (bottom) measured in a few representative spectral lines
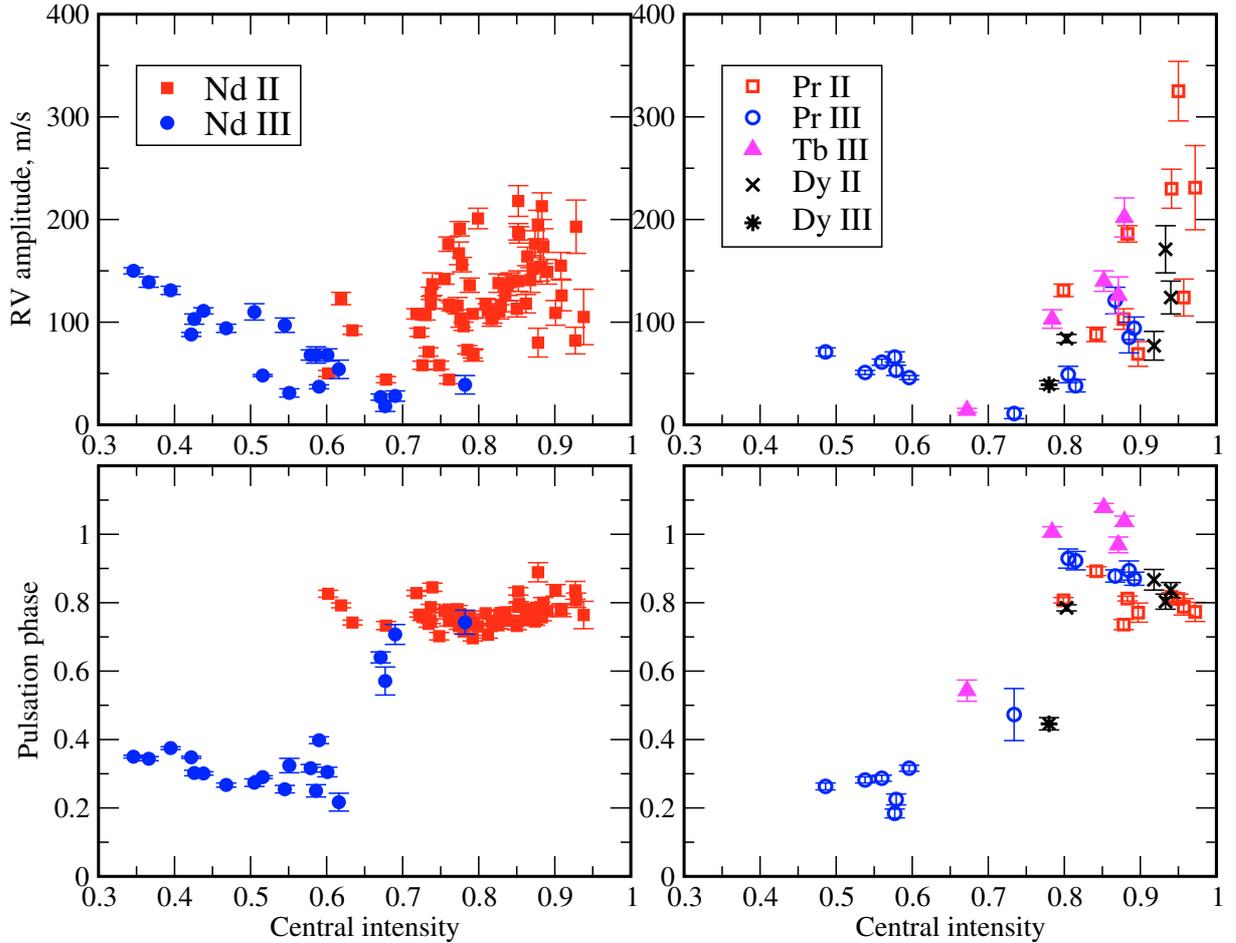
Fig. 20. Amplitude (*top*) and phase (*bottom*) dependence on the central line intensity in the atmosphere of 33 Lib for the main frequency. *Left panels* represent measurements in Nd II- III lines, while *right panels* show the same for other elements with lines in the second and third ionisation states.

for the main period 8.27 min (left panels) and its harmonic (right panels).

We have to emphasise here a major difficulty in the bisector measurements for the lines splitted in strong magnetic field. Figure 22 shows intrinsic theoretical profiles of the lines from Fig. 20, calculated with the abundances that reproduce the observed line intensity. Only the Nd II 5320 Å line does not exhibit resolved Zeeman components in the intrinsic profile, therefore this line may provide the "purest" pulsation distribution across the line profile. Unfortunately, no strong Nd III or Pr III line has negligible Zeeman splitting. The best and strongest Pr III 5300 Å and Nd III 5294 Å lines both have significant splitting and rather different Zeeman patterns. Moreover, the Nd III 5294 Å line is blended in both wings, and these blends may distort the observed pulsation effects. In particular, it concerns the RV amplitudes and, to a lesser extent, pulsation phases. Therefore we chose another Nd III 6327 Å line as a representative of Nd III strong lines. Note that spectral lines with similar Zeeman patterns and similar intensities (Nd III 5677, 5802, 5851 Å) have the same bisector velocity amplitude and phase distributions. Pulsation phases are still similar for the lines with similar Zeeman patterns but with different intensities (Nd III 6327 Å and Pr III 5300 Å). Therefore, here we discuss mainly pulsation phase distribution in the atmosphere of 33 Lib.

Across the profiles of all strong Pr III and Nd III lines and the Nd II 5320 Å line, one phase jump is observed for the main

period and two phase jumps are detected for the first harmonic. Kurtz et al. (2005b) find only one phase jump for the first harmonic using bisector measurements of the Nd III 6145 Å line. The best pulsation distribution is defined by the bisector measurements in the Pr III 5300 Å line, where it is clearly seen that the position of the phase jumps corresponds to nearly zero RV amplitudes, indicating two radial nodes.

Due to the diversity of the pulsational characteristics, it is difficult to compare pulsation phases for the lines of different species. However, a phase distribution for the main period (Fig. 20, bottom left panel) suggests the existence of the π-radian jump between Nd II and Nd III lines, which was found earlier by Mkrtichian et al. (2003), and another π-radian jump between the Eu II 6645 Å and Dy III 5730 Å lines. Comprehensive analysis of the variability of many REE lines in 33 Lib allowed us to obtain a refined picture of the pulsation node in high atmospheric layers. In particular, we show (see Fig. 20, upper panel) that Nd II and Nd III lines do not simply show a π-radian phase difference, but a continuous phase trend exists in the RV curves of Nd III lines, with some of the doubly ionised Nd lines (e.g., 5286 and 6690 Å) pulsating with phases typical of Nd II. This appears to be the first demonstration of the existence of a pulsation node within the formation region of the lines belonging to the same REE ion. Another remarkable observation that we made is that harmonic RV variations are the strongest in the lines that form close to the position of the node. Thus, the mechanism exciting
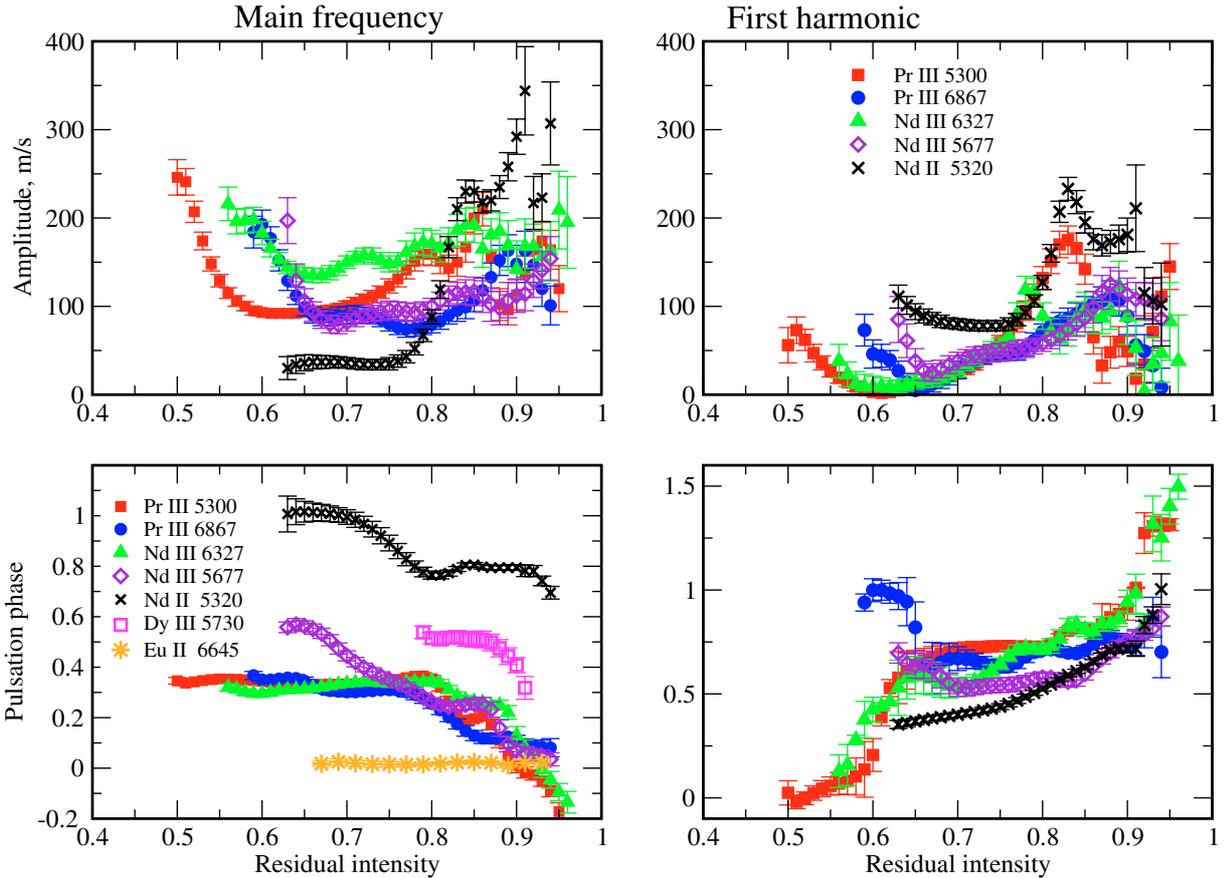
Fig. 21. Amplitude-phase diagrams for the pulsation bisector measurements in 33 Lib. Amplitudes and phases are shown for the main period 8.27 min (*left panels*) and its first harmonic (*right panels*).

the first harmonic is probably directly related to the presence of a radial node in the upper atmosphere of 33 Lib.

The phases of the Hα core lie between the phases of the Eu II line and the wing of the Dy III 5730 Å line. Interestingly, the very core of Hα has the highest RV amplitude, 500 m s⁻¹, and the last measured point in the Dy III line wing has very high RV amplitude, too, although this measurement is not accurate enough. Nevertheless, this gives us a hint of the line formation depths in the atmosphere of 33 Lib. Without detailed analysis of the chemical structure of the atmosphere, it is difficult to suggest a pulsational scenario for the star, but it is evident that we observe several waves over the whole atmosphere.

The phase distribution across the Pr III and Nd III spectral lines allows us to estimate the pulsation wave speed. Assuming that we have one full harmonic wave over the Nd III and Pr III lines and considering the geometric size of the line-formation region in the stratified case (Mashonkina et al. 2005; Ryabchikova et al. 2006b), we estimated the pulsation wave speed as less than 6 km s⁻¹ for the harmonic period 4.136 min. It is lower than the sound speed in the 33 Lib atmosphere in adiabatic approximation and is similar to the pulsation wave speed in another roAp star, HD 24712 (Ryabchikova et al. 2007). The magnetic field, which is stronger in 33 Lib than in any other programme star, may be a reason for the difference in the observed distribution of the pulsational characteristics over the atmospheres of 33 Lib and HD 24712.

What conclusions can be made from these results? Calculations of linear and non-linear radial pulsations (for example, Fadeev & Fokin 1985) in adiabatic approximation show

that the wave speed may differ from the sound speed because of the reflection conditions and of the finite amplitude. Therefore, our results cannot give any proof of the non-adiabaticity of the pulsations in roAp stars. However, that the pulsation wave speed is close to the sound speed strongly supports an acoustic nature for the pulsations and an absence of the shock waves.

While no extra broadening is required to fit the Fe-peak lines, 3−4 km s⁻¹ is necessary for Y II, Eu II, Gd II, and Er II lines. For Nd II and weak Nd III and for Pr III lines, one needs 6−8 km s⁻¹, and, finally, for the strong Nd III and Pr III lines we have to introduce $V_{macro} = 10-12$ km s⁻¹ to fit the observed profiles.

Rather high amplitude pulsations were detected in both Th III lines with the phases corresponding to those for Tb III lines. The RV amplitudes of the main frequency derived for the lines of Na, Mg, Si, Ca, Sc Cr, Ti, Fe, Ni lie in the 30−50 m s⁻¹ range, while the amplitude of the harmonic is below the detection limit of ∼10 m s⁻¹. The Ba lines also reveal pulsations at the main frequency, but with higher RV amplitudes (70−100 m s⁻¹). The Y II lines have similar amplitudes, which seem to grow with the line intensity. The Y II lines also show detectable harmonic amplitudes. All these lines show pulsation phases in the range of pulsation phases for the singly ionised REEs.

7. Summary and discussion

We have analysed spectroscopic pulsational variability of ten roAp stars in detail. For each object, several hundred spectral lines were measured and the resulting time series of radial velocity and bisector variation of selected lines were interpreted
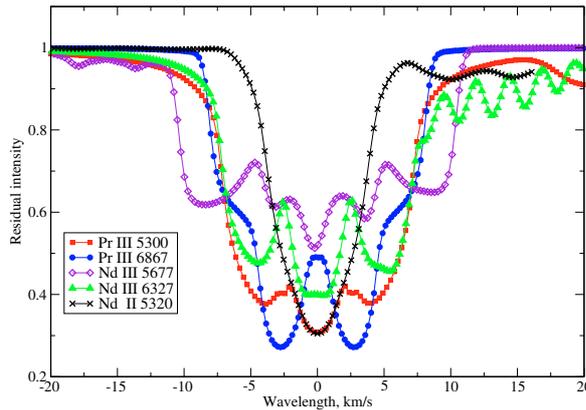
Fig. 22. Zeeman structure for a set of REE spectral lines in 33 Lib.

with the help of the least-square fitting technique. We confirm results of the previous studies, which suggest that non-radial oscillations are primarily detectable in the lines of heavy elements, especially in the doubly ionised REE lines. This phenomenon is attributed to the extreme chemical stratification present in the atmospheres of cool Ap stars. Due to the segregation of elements under the influence of radiative diffusion and due to lack of mixing, a thin layer enriched in heavy elements is created in the upper atmosphere, where rather weak roAp non-radial oscillations attain significant amplitudes.

Stellar atmosphere modelling that includes stratification, NLTE, and magnetic field effects is an extremely complex problem. Up to now only the first preliminary models of different element distributions over stellar atmosphere based on the spectroscopic observations were calculated for a few cool Ap stars. Self-consistent diffusion calculations (LeBlanc & Monin 2004) provide the next step in our understanding of the Ap star phenomenon. However, with the diffusion calculations for 39 elements from He to La, LeBlanc & Monin's models do not include REE elements, which show the most outstanding stratification signatures in roAp atmospheres. The predicted stratification of La is far from the observed one because a small number of the ionisation states (two) is taken into account and NLTE effects are not considered. Empirically derived Nd abundance distribution shows directly that NLTE effects play a crucial role in the REE stratification studies (Mashonkina et al. 2005). Based on the empirical element distribution in the atmospheres of two roAp stars, HD 24712 and γ Equ, we conclude that pulsation amplitudes and, in particular, phases derived from the lines of different elements correlate with the optical depth. Therefore, in the absence of the proper atmospheric models, the amplitude-phase diagrams proposed in the present paper are a powerful tool in the study of vertical structure of p-modes in the atmospheres of roAp stars.

Our pulsation analysis of the radial velocity variations demonstrates similarity in the atmospheric pulsation characteristics. With the help of amplitude-phase diagram analysis we find that pulsation waves exhibit either a constant phase and amplitude changing with height or depth-dependence of both parameters. We interpret the former as a signature of standing pulsation wave and the latter as evidence of a travelling (running) wave in stellar atmosphere. Thus, in general, atmospheric pulsational fluctuations in roAp stars can be represented by a superposition of standing and running waves. According to our results, pulsation waves in three roAp stars, HD 24712, HD 134214, and α Cir, with the pulsation frequency close to or below the acoustic cut-off limit, have the running-wave character from the low

atmospheric heights. In the longer period stars, standing waves are observed up to some of the atmospheric layers, defined by the formation depth of the lines of specific elements, while running waves dominate higher in the atmosphere.

We also find that the change from the standing to running character of pulsation waves depends on the effective temperature of roAp star. Hotter stars seem to develop the running wave deeper in the atmosphere than the cooler stars with the same pulsation periods.

In all stars but 33 Lib, independent of the atmospheric and pulsation parameters, pulsation measurements reveal waves travelling through the layers defined by the same sequence of chemical species. The lowest amplitudes are observed for Eu II lines, then pulsations propagate in the layers where Hα core, Nd, and Pr lines originate. Pulsation amplitude reaches maximum around these atmospheric heights and then decreases outwards in most stars. The RV extremum of the second REE ions is always observed later in time relative to the variation of singly ionised REEs. The largest phase shifts and amplitudes are often detected in Tb III and Th III lines. Pulsational variability in the latter lines is detected here for the first time. Similarity of the pulsation wave propagation signatures in the studied roAp stars suggests that layers enriched in different REE species are arranged in approximately the same vertical order in all stars. For two stars, 33 Lib and HD 19918, we find weak but definite RV variability in the lines of iron-peak elements, confirming previous results by Mkrtichian et al. (2003) and Kurtz et al. (2005b), respectively.

In all stars, spectral lines with the highest RV amplitudes have an additional broadening varying from 4 to 10–12 km s^{-1} in terms of the macroturbulent velocity required to reproduce the observed line profile shapes. The running wave characteristics usually appear in the lines with $V_{\mathrm{macro}} \geq 10$ km s^{-1}. According to Kochukhov et al. (2007), these are the lines where the usual symmetric pulsational line profile variability is transformed into an asymmetric blue-to-red moving pattern. These authors propose pulsational variability of the line widths, arising from the periodic expansion and compression of the turbulent layers in the upper atmospheres of roAp stars as an explanation for the asymmetric line profile variability pattern. The present study shows that the position of the turbulent layer in the roAp-star atmospheres is defined by the formation depth of Pr III lines in a cooler part of the programme stars and by the formation depth of Nd III lines in hotter stars. This turbulent layer, which is probably related to the REE abundance gradients in the upper atmosphere (Mashonkina et al. 2005), seems to be the key element in the depth-dependence of the spectroscopic pulsation characteristics in roAp stars. Abundance gradients may cause a non-standard temperature structure in Ap-star atmospheres. This is supported by an atmospheric anomaly that required to explain the peculiar core-wing transition of the Balmer lines (Kochukhov et al. 2002). Therefore, the comprehensive investigation of the roAp-star atmosphere, including chemical diffusion and magnetohydrodynamic modelling of the interaction of convection, pulsation and magnetic field, is necessary to fully understand the full variety of the phenomena associated with a turbulent REE-rich cloud in cool Ap stars.

One of the sample stars, 33 Lib, differs from all other roAp stars in that, at a given atmospheric heights, it shows a comparable RV amplitude of the main frequency and its first harmonic. Comprehensive analysis of the REE lines of several elements in both ionisations stages shows that harmonic oscillation emerges close to the position of the pulsation node located within the REE-rich high atmospheric layer. This follows from the observation that the lines showing large double-wave

variation are all located close to the minimum amplitude and to a π-radian phase jump of the main frequency. Thus, the physical mechanism giving rise to harmonic spectroscopic variability in 33 Lib must be closely related to the existence of the radial node.

Based on the observation of the two radial nodes for the harmonic variation across the profiles of a few strongest Nd III and Pr III lines, we can estimate a radial wavelength and pulsation wave speed. The latter is below the adiabatic sound speed in the atmosphere of 33 Lib. The same result was obtained earlier for another roAp star, HD 24712, using a different approach (Ryabchikova et al. 2007). These results support an acoustic nature for the pulsations and reject the idea of the shock wave proposed by Shibahashi et al. (2004) for interpreting of the blue-to-red pulsation pattern, because this model requires supersonic pulsation motions.

33 Lib is the only star showing definite and direct evidence of radial nodes in the atmosphere. But the absence of a measurable pulsation signal in the lines of the elements with $Z \leq 38$ in most of our programme stars poses a question about the existence of another node in the lower photospheric layers. Abundance stratification analyses of cool Ap stars (Ryabchikova et al. 2002, 2005b; Kochukhov et al. 2006), as well as the model atmosphere with self-consistent diffusion calculations (LeBlanc & Monin 2004), show that light and iron-peak elements have a tendency to concentrate in the deeper atmosphere, below $\log \tau_{5000} = -1$, and to be strongly depleted in the outer atmospheric layers. Therefore, practically all Fe-peak lines observed in the optical spectral region are formed in the layers $-1.5 < \log \tau_{5000} < 0.0$. The non-adiabatic theoretical pulsation model for HD 24712 supports the existence of the nodal region near the photosphere ($\log \tau_{5000} \sim 0$) (see Fig. 3 in Sachkov et al. 2006). The position of the radial node depends on the frequency (or the radial order) of the mode. As the frequency increases, the node shifts outwards (Saio, private communication). According to this model, in the roAp stars HD 24712, HD 134214, and α Cir, the node is located close to, or slightly above, the continuum-forming layers. On the other hand, in the longer-period stars the node should be located below the photosphere (see Figs. 3, 4 in Saio & Gautschy 2004; Fig. 8 in Saio 2005). For some intermediate pulsation frequencies, we should detect pulsation signal in the region of the iron-peak line formation, but this is not observed. Perhaps, the pulsation amplitude in the lower atmosphere is diminished to such an extent that pulsations are undetectable even in anti-node regions.

A discovery of the low-amplitude pulsations in Y II lines in phase with the highest-amplitude Pr III lines delineates another problem. In the three stars with the shortest pulsation periods, HD 24712, HD 134214, and α Cir, the Y II lines produce a secondary minimum in the amplitude-phase diagrams. These lines have the lowest detected RV amplitudes and are out of phase by π-radian with some other low-amplitude lines, for instance, Eu II. Does this indicate a radial node near the Eu II line formation heights or do we see a double-wave structure in the amplitude-phase diagram depending on the chemical structure of stellar atmospheres?

The amplitude-phase diagrams derived for as many elements and spectral lines as possible are proven to be an extremely powerful tool for investigating the pulsation properties of roAp atmospheres. Detailed inferences about the vertical mode structure obtained in our study call for in-depth theoretical investigation of the propagation of pulsation waves in magnetically dominated and chemically stratified atmospheres. The most important and difficult theoretical challenge is to recognise and model the physical processes that are responsible for remarkable observation of

pulsation wave transformation in the REE-rich layer. Why does the dominant character of pulsational perturbation changes from standing to running wave? What causes pulsation amplitude to diminish about certain atmospheric height? Why does isotropic turbulence increase dramatically in this layer? And finally, what is the origin of the complex bisector behaviour observed in several roAp stars? Substantial theoretical developments are needed to resolve these issues.

References

Audard, N., Kupka, F., Morel, P., Provost, J., & Weiss, W. W. 1998, A&A, 335, 954

Babel, J. 1992, A&A, 258, 449

Baldry, I. K., & Bedding, T. R. 2000, MNRAS, 318, 341

Baldry, I. K., Bedding, T. R., Viskum, M., Kjeldsen, H., & Frandsen, S. 1998, MNRAS, 295, 33

Balona, L. A. 2002, MNRAS, 337, 1059

Biémont, E., Palmeri, P., & Quinet, P. 1999, Ap&SS, 635, 2691

Burki, G., et al. 2005, GENEVA photometric database, Geneva Observatory

Cowley, C. R., Ryabchikova, T., Kupka, F., et al. 2000, MNRAS, 317, 299

Cowley, C. R., Hubrig, S., Ryabchikova, T., et al. 2001, A&A, 367, 939

Den Hartog, E. A., Lawler, J. E., Sneden, C., & Cowan, J. J. 2003, ApJS, 148, 543

Den Hartog, E. A., Lawler, J. E., Sneden, C., & Cowan, J. J. 2006, ApJS, 167, 292

Elkin, V. G., Kurtz, D. W., & Mathys, G. 2005, MNRAS, 364, 864

Fadeev, Yu. A., & Fokin, A. V. 1985, Ap&SS, 111, 355

Hauck, B., & Mermilliod, M. 1998, A&AS, 129, 431

Horne, J. H., & Baliunas, S. L. 1986, ApJ, 302, 757

Kanaan, A., & Hatzes, A. P. 1998, ApJ, 503, 848

Kochukhov, O. 2004, ApJ, 615, L149

Kochukhov, O. 2005, A&A, 438, 219

Kochukhov, O. 2006a, in Magnetic Stars 2006, ed. I. I. Romanyuk, & D. O. Kudryavtsev, in press

Kochukhov, O. 2006b, Comm. Asteroseismol., 149, in press

Kochukhov, O., & Ryabchikova, T. 2001a, A&A, 374, 615

Kochukhov, O., & Ryabchikova, T. 2001b, A&A, 377, L22

Kochukhov, O., Bagnulo, S., & Barklem, P. S. 2002, ApJ, 578, L75

Kochukhov, O., Ryabchikova, T., & Piskunov, N. 2004, A&A, 415, L13

Kochukhov, O., Tsymbal, V., Ryabchikova, T., Makaganyk, V., & Bagnulo, S. 2006, A&A, 460, 831

Kochukhov, O., Ryabchikova, T., Weiss, W. W., Landstreet, J. D., & Lyashko, D. 2007, MNRAS, in press [arXiv:astro-ph/0612761]

Künzli, M., North, P., Kurucz, R. L., & Nicolet, B. 1997, A&AS, 122, 51

Kurtz, D. W., & Martinez, P. 2000, Baltic Astron., 9, 253

Kurtz, D. W., Sullivan, D. J., Martinez, P., & Tripe, P. 1994, MNRAS, 270, 674

Kurtz, D. W., Elkin, V. G., & Mathys, G. 2005a, in Element Stratification in Stars: 40 Years of Atomic Diffusion, ed. G. Alecian, O. Richard, & S. Vauclair, EAS Publ. Ser., 17, 91

Kurtz, D. W., Elkin, V. G., & Mathys, G. 2005b, MNRAS, 358, L6

Kurtz, D. W., Elkin, V. G., & Mathys, G. 2006, MNRAS, 370, 1274

Kupka, F., Ryabchikova, T. A., Weiss, W. W., et al. 1996, A&A, 308, 886

Kupka, F., Piskunov, N., Ryabchikova, T. A., Stempels, H. C., & Weiss, W. W. 1999, A&AS, 138, 119

Lawler, J. E., Bonvallet, G., & Sneden, C. 2001, ApJ, 556, 452

Lawler, J. E., Den Hartog, E. A., Sneden, C., & Cowan, J. J. 2006, ApJS, 162, 227

LeBlanc, F., & Monin, D. 2004, in The A-Star Puzzle, ed. J. Zverko, W. W. Weiss, J. Žižňovský, & S. J. Adelman (Cambridge University Press), Proc. IAU Symp., 224, 193

Lucke, P. B. 1978, A&A, 64, 367

Lüftinger, T., Kochukhov, O., Ryabchikova, T., Weiss, W. W., & Ilyin, I. 2006, in Magnetic Stars 2006, ed. I. I. Romanyuk, & D. O. Kudryavtsev, in press

Mashonkina, L., Ryabchikova, T., & Ryabtsev, A. 2005, A&A, 441, 309

Mkrtichian, D. E., Hatzes, A. P., & Panchuk, V. E. 2000, in Variable Stars as Essential Astrophysical Tools, ed. C. Ibanoglu (Kluwer Academic Pulishers), 405

Mkrtichian, D. E., Hatzes, A. P., & Kanaan, A. 2003, MNRAS, 345, 781

Moon, T. T., & Dworetsky, M. M. 1985, MNRAS, 217, 305

Napiwotzki, R., Schönberner, D., & Wenske, V. 1993, A&A, 268, 653

Piskunov, N. E. 1999, in 2nd International Workshop on Solar Polarization, ed. K. Nagendra, & J. Stenflo (Kluwer Acad. Publ.), ASSL, 243, 515

Rogers, N. Y. 1995, Comm. Asteroseismol., 78

Ryabchikova, T. A., Landstreet, J. D., Gelbmann, M. J., et al. 1997, A&A, 327, 1137

Ryabchikova, T. A., Savanov, I. S., Hatzes, A. P., Weiss, W. W., & Handler, G. 2000, A&A, 357, 981

Ryabchikova, T. A., Savanov, I. S., Malanushenko, V. P., & Kudryavtsev, D. O. 2001, Astron. Rep., 45, 382

Ryabchikova, T., Piskunov, N., Kochukhov, O., et al. 2002, A&A, 384, 545

Ryabchikova, T., Wade, G., & LeBlanc, F. 2003, in Modelling of Stellar Atmospheres, ed. N. E. Piskunov, W. W. Weiss, & D. F. Gray (ASP), IAU Symp., 210, 301

Ryabchikova, T., Nesvacil, N., Weiss, W. W., Kochukhov, O., & Stütz, Ch. 2004, A&A, 423, 705

Ryabchikova, T., Leone, F., & Kochukhov, O. 2005b, A&A, 438, 973

Ryabchikova T., Wade, G. A., Aurière, M., et al. 2005a, A&A, 429, L55

Ryabchikova, T., Ryabtsev, A., Kochukhov, O., & Bagnulo, S. 2006a, A&A, 456, 329

Ryabchikova, T., Mashonkina, L., Ryabtsev, A., Kildiyarova, R., & Khristoforova, M. 2006b, Comm. Asteroseismol., 149, in press

Ryabchikova, T., Sachkov, M., Weiss, W. W., et al. 2007, A&A, 462, 1103

Sachkov, M., Ryabchikova, T., Kochukhov, O., et al. 2004, in Variable Stars in the Local Group, ed. D. W. Kurtz, & K. R. Pollard, ASP Conf. Ser., 310, 208

Sachkov, M., Ryabchikova, T., Bagnulo, et al. 2006, MemSAI, 77, 397

Saio, H. 2005, MNRAS, 360, 1022

Saio, H., & Gautschy, A. 2004, MNRAS, 350, 485

Savanov, I. S., Malanushenko, V. P., & Ryabchikova, T. R. 1999, Astron. Lett., 25, 802

Shibahashi, H., Kurtz, D. W., Kambe, E., Gough, D. O. 2004, in The A-star Puzzle, ed. J. Zverko, J. Žižňovský, S. J. Adelman, & W. W. Weiss (Cambridge University Press), IAUS 224, IAU Symp., 224, 829

Tsymbal, V., Lyashko, D., & Weiss, W. W. 2003, in Modelling of Stellar Atmiiospheres, ed. N. Piskunov, W. W. Weiss, & D. F. Gray (ASP), IAU Symp., 210, E49

Online Material
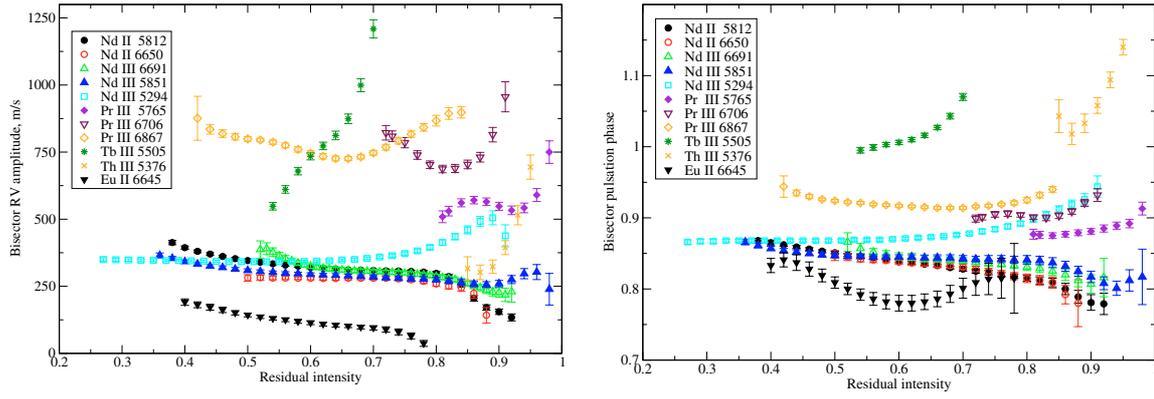
Fig. 5. Bisector measurements as a function of the line residual intensity in HD 101065. *Left panel* represents RV amplitudes, *right panel* shows phases calculated with the main period from Table 2).
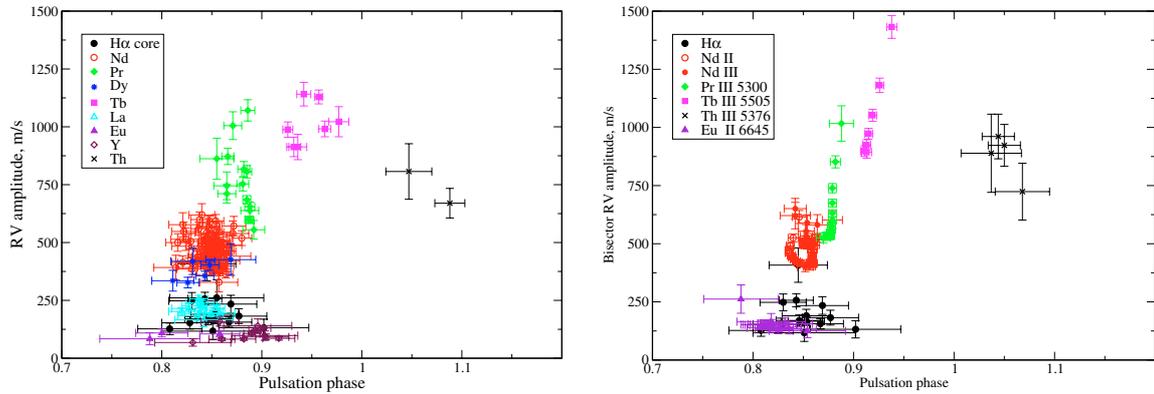
Fig. 6. The same as in Fig. 4 but for HD 122970.
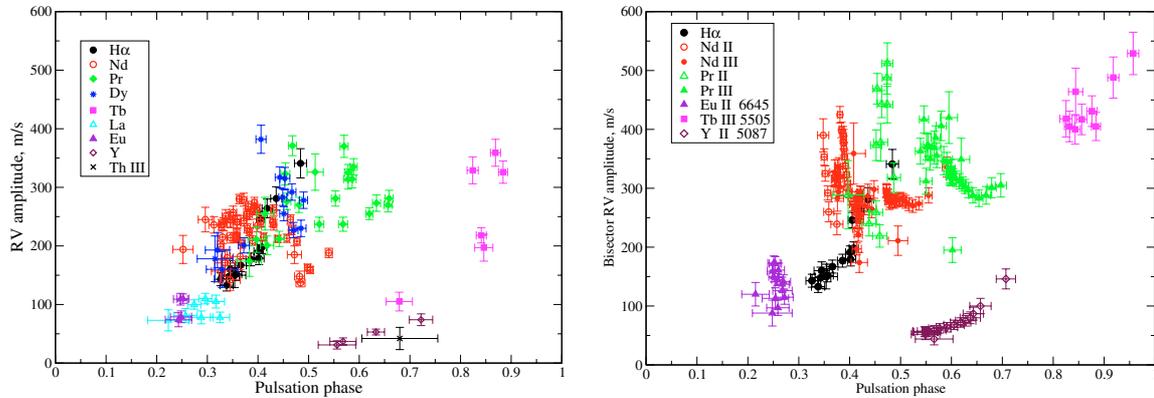
Fig. 8. The same as in Fig. 4 but for HD 24712.
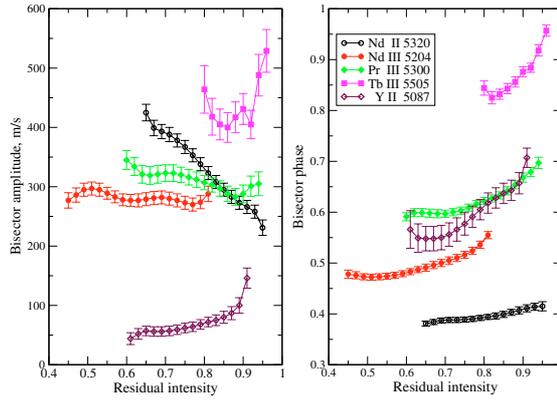
Fig. 9. The same as in Fig. 7 but for HD 24712.
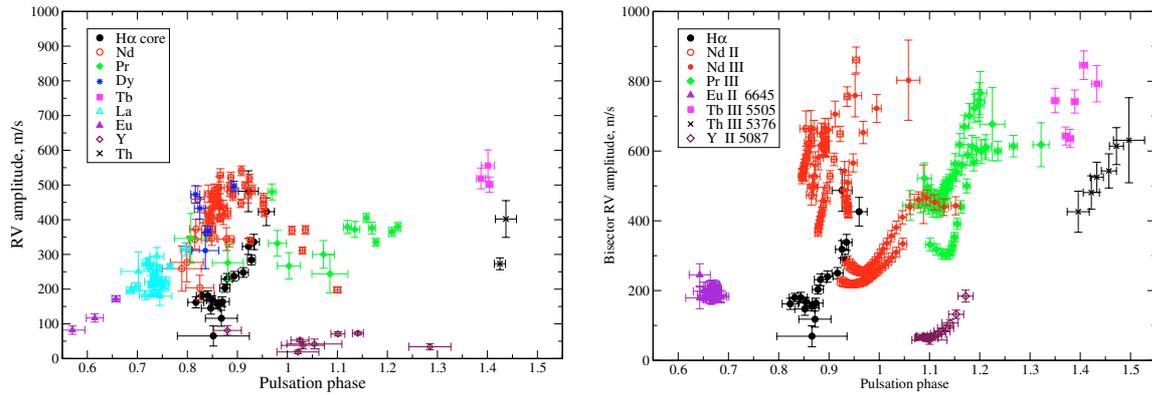
Fig. 10. The same as in Fig. 4 but for HD 134214.
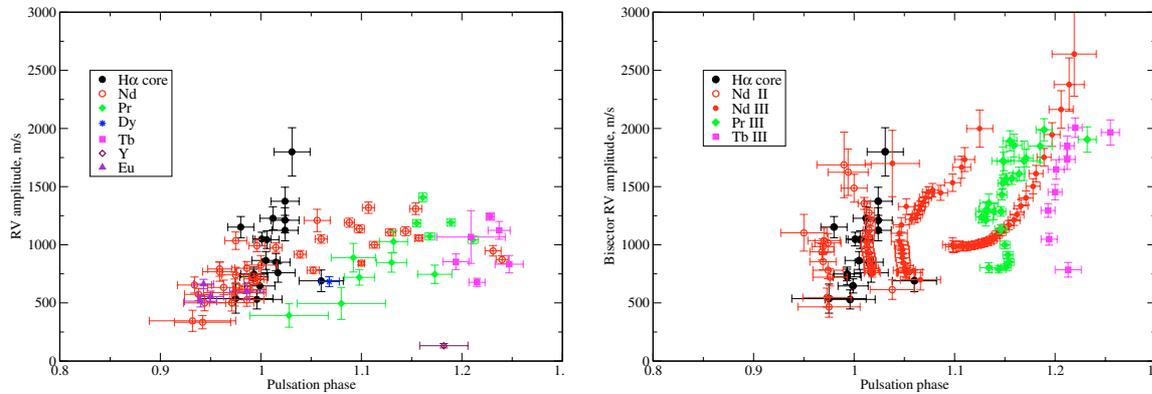
Fig. 12. The same as in Fig. 4 but for HD 12932.
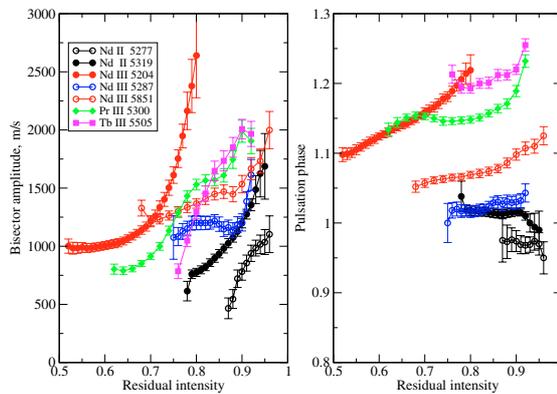
Fig. 13. The same as in Fig. 7 but for HD 12932.
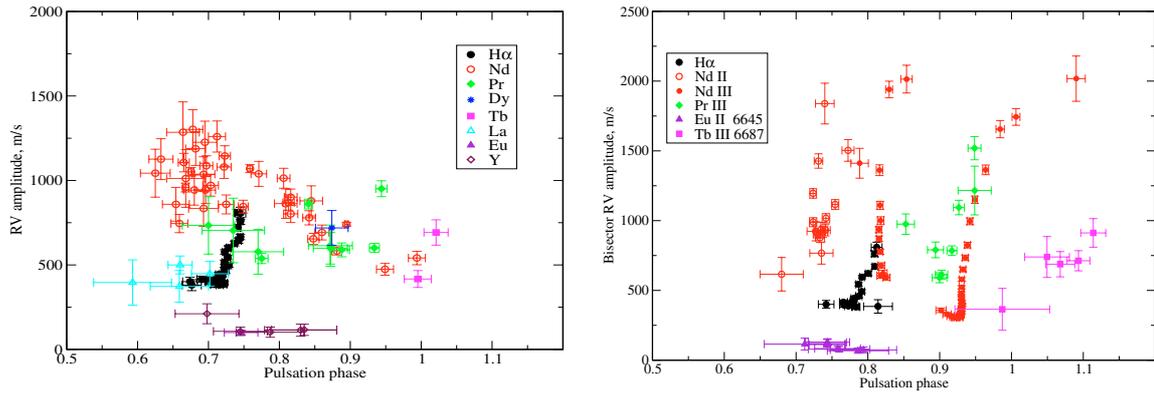
Fig. 15. The same as in Fig. 4 but for γ Equ.
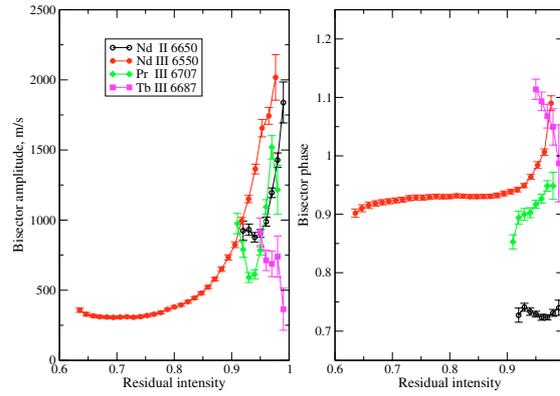
Fig. 16. The same as in Fig. 7 but for HD 201601.
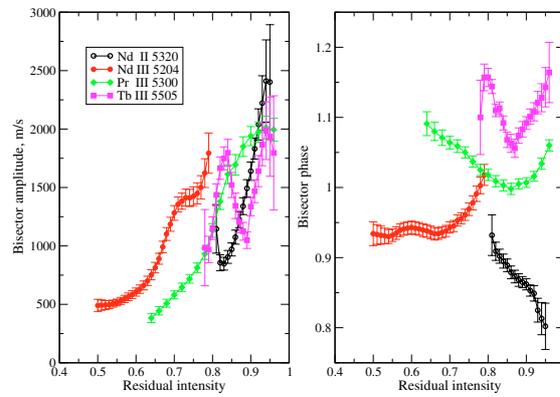
Fig. 17. The same as in Fig. 7 but for HD 19918.
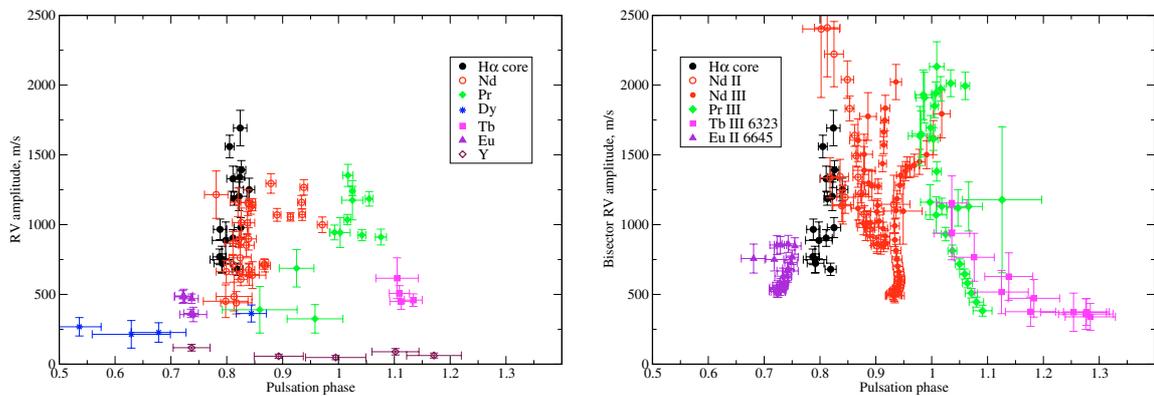
Fig. 18. The same as in Fig. 4 but for HD 19918.

Table 3. Pulsation amplitudes (first line) and phases (second line) calculated with the period highlighted with italics in Table 2. Errors in the last digits are given in paranthesis. When no pulsation signal was detected, we give the formal amplitude solution for the fixed period without phase information.

Wavelength (Å)	HD 24712	HD 101065	HD 122970	HD 134214	HD 12932	HD 19918	HD 201601	HD 128898	HD 9289	HD 137949
Fe I - Fe II										
5405.775	7 (5)	7 (4)	14 (4)	11(4)	25 (18)	37 (15) / 0.607 (67)	17 (19)	9 (3)	11(20)	17(2) / 0.686(21)
5410.910	12 (4)		11 (4)	6 (3)	16 (14)	52 (18) / 0.650 (56)	60 (24)	6 (3)	23(12)	14(1) / 0.632(22)
5415.199	8 (4)	21 (7)	2(4)	9 (3)	18(13)	21 (9) / 0.624 (70)	14 (14)	5 (4)	48(23)	13(1) / 0.396(24)
5424.068	4 (4)		6(4)	2 (3)	13(9)	29 (8) / 0.640(46)	31 (18)	2 (5)	38(24)	25(2) / 0.685(14)
5434.524	20 (7)	51 (21)	9 (7)	4 (3)	7 (15)	47 (19) / 0.665 (65)	38 (25)	11 (6)	95 (44)	27(2) / 0.669(15)
5576.089	15 (10)		27 (10)	13 (4)	35 (15)	100 (43) / 0.778 (69)	33 (27)	11 (8)	126 (41)	22(2) / 0.642 (16)
5414.073	18 (13)	11(14)	5(8)	17 (8)	30 (17)	34 (9) / 0.707 (41)	50 (31)	6 (6)	24(23)	17(2) / 0.552(26)
5425.257	36 (12)		24 (8)	11 (6)	41(12)	35 (17) / 0.545 (77)	65 (23)	23 (11)	48(34)	25(3) / 0.593 (21)
6247.557		13 (11)	1(5)	34(14)	63(13)	29(7) / 0.722(43)		44(9)	42(43)	35(3) / 0.646 (15)
Y II										
3549.005	74 (10) / 0.722 (23)									
4883.684							102 (30) / 0.657 (48)			
4982.129	19 (8)	69 (18) / 0.824 (42)				86 (55)				
5087.416	53 (5) / 0.633 (17)		120 (4) / 0.893 (6)	73 (5) / 1.141 (11)	132 (19) / 1.182 (24)	89 (23) / 1.102 (42)	114 (36) / 0.700 (51)	109 (8) / 0.596 (12)	133 (30) / 0.623 (36)	61 (2) / 0.609 (8)
5119.112	17 (7)		27 (18)	38 (10) / 1.031 (43)						
5123.211			82 (6) / 0.860 (13)							
5200.406			86 (8) / 0.917 (16)			62 (18) / 1.171 (49)				
5205.724			107 (5) / 0.890 (8)			57 (15) / 0.893 (44)				
5402.774	29 (6)		92 (13) / 0.904 (23)	53 (5) / 1.025 (18)			211 (59) / 0.568 (45)			78 (4) / 0.688 (9)
5473.388			68 (16) / 0.831 (38)							
5509.895	31 (7) / 0.556 (37)	36 (6) / 1.012 (27)	83 (6) / 0.882 (12)	19 (5) / 1.021 (42)					66 (27) / 0.489 (66)	49 (3) / 0.610 (10)
5544.611				34 (9) / 1.285 (42)			113 (57) / 0.833 (80)			
5546.009						118 (24) / 0.737 (33)				94 (4) / 0.723 (7)
5662.925	37 (6) / 0.568 (26)		131 (6) / 0.901 (8)	71 (6) / 1.101 (14)		48 (16) / 0.995 (54)	107 (25) / 0.615 (38)	121 (3) / 0.604 (4)	49 (16) / 0.584 (52)	98 (3) / 0.677 (6)
5728.890			140 (30) / 0.896 (34)	42 (14) / 1.054 (55)				56 (21)		104 (7) / 0.640 (11)
6613.733			98 (20) / 0.903 (33)					77 (12) / 0.589 (25)		
6795.414			158 (19) / 0.858 (19)	81 (14) / 0.880 (28)				59 (14) / 0.477 (39)		73 (8) / 0.657 (1)
La II										
4804.039	110 (9) / 0.296 (13)						373 (94) / 0.529 (41)			
4921.776							500 (53) / 0.530 (17)			
4986.819	78 (9) / 0.325 (19)									
5114.559			257 (15) / 0.837 (9)	265 (6) / 0.765 (4)						
5122.988			217 (12) / 0.854 (9)							
5157.433			183 (23) / 0.836 (20)	235 (9) / 0.734 (7)						
5163.611			226 (27) / 0.839 (19)	207 (11) / 0.697 (9)						
5259.379			227 (20) / 0.841 (14)	196 (9) / 0.686 (8)						
5290.818				188 (9) / 0.733 (8)			448 (73) / 0.572 (26)			
5303.528	100 (8) / 0.274 (13)		194 (14) / 0.849 (12)	219 (9) / 0.744 (7)						
5340.655				188 (11) / 0.739 (10)						
5377.052				260 (8) / 0.744 (5)						
5458.697				315 (19)						

Table 3. continued.

Wavelength (Å)	HD 24712	HD 101065	HD 122970	HD 134214	HD 12932	HD 19918	HD 201601	HD 128898	HD 9289	HD 137949
				0.796 (9)						
5482.268				221 (18) 0.727 (13)						
5566.925		121 (6) 0.849 (9)								
5797.565			202 (16) 0.820 (13)							
5805.773		126 (5) 0.833 (7)	239 (20) 0.838 (14)	224 (12) 0.756 (9)			396 (134) 0.463 (55)			111 (9) 0.662 (13)
5808.313		66 (6) 0.834 (14)	215 (22) 0.827 (17)	261 (15) 0.731 (9)						174 (10) 0.630 (9)
5863.691				235 (13) 0.740 (9)						
5880.633		94 (6) 0.814 (10)		213 (15) 0.733 (11)						
5936.210				273 (15) 0.718 (9)						154 (9) 0.704 (10)
6100.374			166 (30) 0.842 (29)	183 (13) 0.715 (11)						
6129.556		56 (6) 0.815 (17)								
6146.523				180 (27) 0.745 (24)						
6262.287	81 (12) 0.257 (23)									198 (12) 0.672 (10)
6296.079	105 (11) 0.317 (17)									
6310.912		46 (5) 0.789 (20)								
6320.376	78 (11) 0.288 (23)		195 (18) 0.858 (15)	213 (8) 0.730 (6)						114 (7) 0.634 (10)
6358.105		88 (4) 0.809 (8)								
6390.477				205 (11) 0.754 (9)						
6399.030	73 (18) 0.223 (41)	74 (9) 0.821 (21)		295 (25) 0.739 (14)						177 (16) 0.643 (15)
6642.755				274 (17) 0.723 (10)						111 (7) 0.660 (10)
6808.885				251 (56) 0.702 (35)						
Pr II										
5070.023		175 (11) 0.863 (10)								88 (7) 0.892 (13)
5110.760	200 (12) 0.446 (10)									
5129.533	243 (11) 0.477 (8)									
5135.140	313 (16) 0.454 (9)		745 (60) 0.865 (13)	332 (37) 0.980 (18)		329 (136) 0.940 (65)	734 (170) 0.570 (37)			
5207.895		310 (7) 0.867 (4)								
5219.045			555 (40) 0.892 (11)							
5292.619	195 (18) 0.400 (14)									131 (6) 0.807 (8)
5321.817		149 (5) 0.852 (6)								
5322.772	368 (18) 0.468 (8)	493 (6) 0.895 (2)	872 (35) 0.866 (6)	480 (23) 0.969 (8)	392 (101) 1.028 (39)	390 (167) 0.859 (67)	704 (191) 0.605 (44)			
5432.038		2215 (10) 0.818 (8)								
5519.388		308 (10) 0.836 (6)								
5605.642		337 (6) 0.843 (3)		276 (53) 0.881 (31)						
5608.931		359 (5) 0.821 (7)								69 (12) 0.771 (28)
5681.901	159 (44) 0.355 (44)			346 (72) 0.807 (33)						325 (29) 0.811 (14)
5786.166		460 (17) 0.871 (6)								
5879.260		382 (9) 0.856 (4)								
5939.899		436 (10) 0.872 (4)								
6017.767	170 (28) 0.385 (26)									
6148.243		378 (18) 0.841 (8)								
6165.891	251 (14) 0.456 (9)	404 (8) 0.860 (3)	711 (40) 0.865 (9)	267 (38) 1.003 (23)						186 (8) 0.812 (7)
6197.452		392 (26) 0.829 (11)								

Table 3. continued.

Wavelength (Å)	Amplitude (m s⁻¹) / Phase (period fraction)									
	HD 24712	HD 101065	HD 122970	HD 134214	HD 12932	HD 19918	HD 201601	HD 128898	HD 9289	HD 137949
6255.098		304 (15) 0.816 (8)								
6656.834	254 (26) 0.419 (17)									
Pr III										
4910.823	248 (11) 0.543 (7)									
5284.693	259 (11) 0.642 (7)	427 (4) 0.934 (2)	600 (14) 0.887 (4)	380 (12 1.221 (5)	1043 (33) 1.211 (5)	925 (40) 1.042 (7)	601 (27) 0.804 (7)	496 (8) 0.692 (3)	504 (21) 0.633 (7)	71 (4) 0.263 (10)
5299.993	246 (10) 0.641 (7)	460 (5) 0.946 (2)	596 (14) 0.888 (4)	365 (13) 1.209 (6)	1192 (32) 1.189 (4)	1185 (52) 1.055 (7)	951 (47) 0.814 (8)	491 (15) 0.684 (5)	724 (30) 0.677 (7)	
5550.593						325 (102) 0.958 (50)				
5765.260		589 (15) 0.895 (4)	1005 (60) 0.871 (9)	300 (40) 1.072 (22)	847 (83) 1.130 (15)	943 (107) 1.003 (18)	578 (133) 0.640 (36)	420 (66) 0.587 (25)	906 (173) 0.581 (31)	85 (15) 0.894 (28)
5844.408	299 (15) 0.576 (8)	398 (7) 0.918 (3)	753 (30) 0.881 (6)	379 (19) 1.120 (8)	746 (79) 1.173 (17)	911 (57) 1.076 (10)	599 (94) 0.742 (24)	414 (37) 0.677 (15)	490 (54) 0.591 (18)	11 (5) 0.473 (76)
5956.050	211 (8) 0.616 (7)						589 (41) 0.758 (11)			
5998.968	329 (15) 0.587 (8)						614 (122) 0.742 (31)			
6053.004	307 (12) 0.583 (7)									
6090.010	265 (12) 0.631 (8)		685 (18) 0.885 (4)		1072 (31) 1.168 (5)					46 (2) 0.316 (9)
6160.233	251 (10) 0.624 (6)		655 (19) 0.888 (5)	376 (17) 1.169 (7)	1408 (39) 1.161 (4)	1241 (34) 1.025 (4)		441 (14) 0.666 (5)	752 (43) 0.679 (9)	53 (5) 0.225 (16)
6195.621	272 (12) 0.626 (7)			335 (11) 1.177 (5)	1185 (32) 1.155 (4)	1036 (37) 1.016 (6)		481 (13) 0.676 (4)	734 (91) 0.723 (20)	61 (3) 0.287 (9)
6429.265		352 (9) 0.902 (4)								
6500.044	244 (12) 0.527 (8)		638 (37) 0.888 (9)		720 (67) 1.098 (15)	944 (53) 0.993 (9)				
6578.901		531 (8) 0.893 (3)	1071 (46) 0.886 (7)		889 (123) 1.092 (22)	1175 (141) 1.025 (19)			792 (139) 0.561 (28)	
6692.247	317 (27) 0.501 (14)	418 (15) 0.884 (6)	862 (89) 0.855 (17)	244 (55) 1.085 (36)	495 (137) 1.080 (44)	687 (134) 0.925 (31)		689 (234) 0.655 (53)		94 (11) 0.870 (19)
6706.704	359 (15) 0.569 (7)	530 (10) 0.918 (3)	817 (33 0.882 (6)	372 (23) 1.135 (10)	1027 (93) 1.132 (14)	1353 (79) 1.017 (9)		553 (52) 0.630 (15)	773 (118) 0.608 (25)	49 (8) 0.929 (28)
6866.794		527 (4) 0.927 (1)	806 (27) 0.885 (5)	405 (13) 1.158 (5)				816 (18) 0.673 (4)		66 (5) 0.184 (13)
Nd II										
3375.244	182 (23) 0.365 (20)									
4706.543							858 (56) 0.595 (11)			
4797.153	205 (9) 0.368 (7)									
4799.420	214 (9) 0.346 (7)									
4811.342	274 (9) 0.393 (5)						1087 (59) 0.567 (9)			
4947.020							1302 (117) 0.548 (14)			
4959.119	254 (9) 0.383 (6)									
4987.161			422 (28) 0.840 (11)							
4989.950	280 (8) 0.363 (5)		519 (32) 0.880 (10)			1157 (92) 0.838 (13)	1260 (92) 0.582 (12)			
5027.847		239 (7) 0.841 (5)								
5033.507	257 (11) 0.351 (7)	221 (5) 0.851 (4)	548 (40) 0.822 (12)	528 (19) 0.866 (6)	825 (82) 1.000 (16)		1037 (103) 0.563 (16)	659 (63) 0.362 (15)	399 (81) 0.604 (33)	203 (10) 0.733 (8)
5077.154	199 (9) 0.326 (7)	167 (4) 0.841 (4)	571 (42) 0.872 (12)	475 (25) 0.842 (8)			1226 (125) 0.565 (17)			137 (8) 0.735 (10)
5089.832	214 (8) 0.358 (6)		437 (18) 0.843 (7)				834 (105) 0.563 (21)			72 (3) 0.747 (8)
5092.794	255 (9) 0.378 (6)		417 (17) 0.840 (6)	495 (13) 0.885 (4)	992 (52) 0.996 (8)	895 (58) 0.822 (10)	943 (80) 0.566 (14)			59 (4) 0.705 (11)
5096.516	236 (9) 0.328 (6)	239 (2) 0.842 (2)	593 (28) 0.854 (8)	453 (19) 0.857 (7)	500 (68) 0.944 (21)	440 (80) 0.817 (28)				117 (6) 0.770 (9)
5105.226			439 (22) 0.838 (8)							193 (7) 0.768 (6)
5130.586	261 (8) 0.398 (5)	208 (2) 0.855 (2)	448 (13) 0.858 (5)	499 (10) 0.915 (3)	976 (40) 1.015 (6)	1131 (56) 0.843 (8)	1145 (60) 0.593 (8)	773 (17) 0.362 (4)	415 (36) 0.576 (14)	
5132.328	279 (11) 0.372 (6)		477 (23) 0.862 (8)	522 (15) 0.887 (5)	707 (48) 0.993 (10)	898 (80) 0.839 (14)				117 (3) 0.778 (5)
5143.337	237 (11) 0.332 (7)	234 (3) 0.827 (3)	599 (33) 0.838 (9)	404 (23) 0.850 (9)	502 (72) 0.971 (22)		1012 (171) 0.538 (27)			
5152.62			416 (55) 0.835 (21)	277 (56) 0.799 (33)						

Table 3. continued.

Wavelength (Å)	HD 24712	HD 101065	HD 122970	HD 134214	HD 12932	HD 19918	HD 201601	HD 128898	HD 9289	HD 137949
5165.129	214 (8)	205 (3)	374 (18)	443 (11)	618 (34)	676 (48)				44 (4)
	0.356 (6)	0.857 (3)	0.857 (8)	0.864 (4)	0.981 (9)	0.839 (11)				0.750 (14)
5167.919		244 (5)								
		0.823 (3)								
5176.781	215 (11)		436 (28)			663 (81)				
	0.330 (8)		0.849 (10)			0.799 (18)				
5181.169		234 (3)								71 (4)
		0.847 (2)								0.741 (10)
5182.587	251 (11)					714 (72)	745 (54)			158 (7)
	0.336 (7)					0.811 (16)	0.529 (12)			0.758 (7)
5192.614		197 (3)								
		0.849 (3)								
5212.361		291 (4)	440 (18)							91 (4)
		0.843 (3)	0.845 (6)							0.766 (7)
5255.506	263 (9)	292 (4)	440 (13)							59 (4)
	0.391 (5)	0.846 (2)	0.844 (5)							0.762 (11)
5276.869	219 (8)		516 (21)	489 (13)	792 (62)		971 (64)		314 (53)	120 (5)
	0.358 (6)		0.844 (7)	0.862 (4)	0.959 (12)		0.573 (11)		0.611 (27)	0.787 (8)
5287.133		239 (4)								
		0.834 (3)								
5293.163			387 (15)					858 (28)		
			0.855 (6)					0.391 (5)		
5306.460		228 (3)	544 (26)	446 (15)	633 (63)					
		0.849 (2)	0.854 (8)	0.859 (6)	0.963 (16)					
5311.453	243 (9)	207 (2)	493 (21)	482 (14)	798 (58)	1160 (102)		785 (32)	572 (121)	97 (4)
	0.372 (6)	0.839 (2)	0.843 (7)	0.885 (5)	0.986 (12)	0.820 (14)		0.323 (7)	0.599 (34)	0.719 (8)
5314.554	236 (14)	210 (4)	514 (48)	391 (28)						151 (12)
	0.313 (10)	0.839 (3)	0.824 (15)	0.837 (12)						0.776 (13)
5319.815	262 (9)	209 (3)	434 (13)	519 (12)	1000 (29)	1142 (43)	1079 (67)	793 (15)	609 (5)	125 (5)
	0.398 (5)	0.847 (3)	0.846 (5)	0.924 (4)	1.113 (5)	0.846 (6)	0.592 (10)	0.356 (3)	0.545 (14)	0.793 (7)
5356.967	241 (10)	181 (4)	485 (23)		1035 (75)			858 (35)	603 (78)	
	0.359 (7)	0.847 (4)	0.848 (7)		0.975 (11)			0.323 (6)	0.605 (21)	
5361.467	224 (7)		412 (35)					416 (18)	341 (48)	
	0.383 (5)		0.830 (14)					0.319 (7)	0.493 (23)	
5371.927		242 (4)	459 (23)	469 (14)	701 (38)	706 (45)	1188 (99)			
		0.839 (3)	0.852 (8)	0.891 (5)	0.997 (9)	0.868 (10)	0.552 (14)			
5385.888		243 (4)	542 (40)	463 (21)	654 (69)	641 (76)		577 (55)		
		0.830 (3)	0.845 (12)	0.860 (7)	0.934 (17)	0.840 (18)		0.309 (15)		
5399.099		217 (6)	565 (39)	373 (28)			1043 (142)			
		0.826 (4)	0.847 (11)	0.817 (12)			0.495 (21)			
5416.374		222 (4)	560 (28)	467 (14)		852 (80)	943 (89)	592 (61)		112 (7)
		0.854 (3)	0.837 (8)	0.850 (5)		0.835 (14)	0.550 (15)	0.288 (17)		0.710 (10)
5430.780		244 (6)	441 (67)							
		0.830 (4)	0.865 (24)							
5431.516			422 (36)	418 (15)	615 (61)	762 (96)	1285 (180)	718 (49)		168 (10)
			0.864 (14)	0.881 (6)	0.989 (16)	0.824 (20)	0.534 (23)	0.314 (11)		0.733 (10)
5442.264		201 (3)	447 (19)							
		0.847 (2)	0.842 (7)							
5456.553							859 (100)		313 (85)	103 (6)
							0.524 (19)		0.538 (44)	0.749 (11)
5474.731		198 (4)	535 (38)	417 (20)	334 (57)					
		0.847 (4)	0.850 (11)	0.843 (8)	0.942 (28)					
5485.696	230 (8)	226 (6)	483 (27)	484 (18)		1013 (81)		705 (24)	238 (71)	109 (4)
	0.379 (6)	0.839 (4)	0.860 (9)	0.891 (6)		0.837 (13)		0.333 (6)	0.539 (48)	0.736 (6)
5491.390		162 (6)								
		0.806 (6)								
5533.820	245 (13)		500 (38)	492 (32)	589 (99)	1215 (170)	1126 (121)	921 (85)		128 (7)
	0.345 (9)		0.816 (12)	0.863 (11)	0.974 (31)	0.781 (21)	0.503 (17)	0.287 (15)		0.771 (9)
5557.40			505 (35)							164 (8)
			0.829 (11)							0.782 (8)
5569.946		263 (4)								
		0.835 (3)								
5618.994			545 (42)	413 (20)	346 (91)	638 (96)				
			0.857 (12)	0.846 (8)	0.932 (43)	0.846 (24)				
5659.775			401 (19)							
			0.859 (7)							
5687.957		255 (4)								
		0.839 (3)								
5702.238		202 (3)								128 (6)
		0.829 (3)								0.748 (7)
5707.363		221 (7)								
		0.809 (5)								
5718.180		212 (3)	427 (23)							69 (3)
		0.815 (3)	0.854 (9)							0.698 (8)
5726.825				374 (14)	527 (56)					
				0.850 (6)	0.986 (17)					
5734.550	245 (21)	259 (10)	386 (35)	363 (24)		451 (117)		378 (92)		152 (12)
	0.296 (14)	0.833 (7)	0.830 (15)	0.845 (11)		0.798 (40)		0.259 (39)		0.750 (13)
5740.858			472 (36)					853 (122)		
			0.844 (12)					0.320 (23)		
5742.087		239 (5)	503 (34)							
		0.835 (4)	0.857 (11)							
5743.193		239 (6)	392 (53)	459 (38)						116 (8)
		0.827 (4)	0.814 (22)	0.821 (13)						0.782 (11)

Table 3. continued.

Wavelength (Å)	HD 24712	HD 101065	HD 122970	HD 134214	HD 12932	HD 19918	HD 201601	HD 128898	HD 9289	HD 137949
5744.777								508 (59) 0.266 (19)	477 (156) 0.432 (53)	139 (9) 0.749 (10)
5761.694		253 (7) 0.825 (4)		346 (20) 0.849 (10)				487 (88) 0.275 (29)		137 (10) 0.748 (12)
5764.212		221 (6) 0.819 (4)	328 (41) 0.857 (19)							
5804.004				404 (11) 0.865 (5)	573 (52) 0.938 (14)	608 (46) 0.825 (12)			321 (49) 0.512 (25)	108 (4) 0.759 (7)
5811.572		217 (5) 0.826 (4)	588 (26) 0.848 (7)	456 (17) 0.860 (6)	768 (82) 0.959 (17)					
5825.857		215 (4) 0.836 (4)	479 (26) 0.846 (9)	457 (16) 0.851 (6)					286 (85) 0.592 (48)	119 (5) 0.768 (7)
5842.366				338 (16) 0.884 (8)						108 (11) 0.837 (17)
5865.027		252 (7) 0.825 (5)	462 (42) 0.859 (15)	344 (33) 0.878 (16)						142 (11) 0.750 (13)
5891.506		226 (3) 0.831 (3)	417 (28) 0.844 (10)							
5900.406		226 (6) 0.810 (5)								
6082.899		274 (21) 0.812 (12)								
6108.403			394 (35) 0.844 (14)							
6133.957				259 (65) 0.789 (39)						
6210.663	194 (24) 0.252 (20)	230 (9) 0.813 (6)								113 (27) 0.767 (38)
6248.274		241 (7) 0.819 (5)	397 (31) 0.851 (12)	343 (28) 0.815 (13)						158 (13) 0.782 (13)
6250.438		306 (9) 0.814 (5)								
6263.202		255 (11) 0.825 (7)								
6287.20		231 (8) 0.823 (6)		315 (36) 0.805 (19)						
6298.411			399 (32) 0.859 (13)							
6341.492			539 (54) 0.871 (16)							140 (9) 0.790 (11)
6354.75		241 (9) 0.811 (6)								
6365.540		239 (6) 0.814 (4)	619 (49) 0.840 (13)	437 (38) 0.865 (14)						
6465.218	142 (18) 0.345 (20)									127 (14) 0.779 (18)
6492.335			489 (42) 0.867 (13)							
6495.576		214 (6) 0.816 (5)								
6504.464		240 (7) 0.801 (5)								
6514.959	171 (23) 0.335 (21)									
6585.696		191 (5) 0.820 (5)								
6588.020		218 (7) 0.820 (6)								
6637.187	180 (13) 0.339 (12)		523 (43) 0.852 (13)	432 (42) 0.848 (16)				527 (75) 0.233 (24)		174 (16) 0.798 (15)
6637.96	244 (13) 0.346 (9)	219 (6) 0.826 (5)	414 (28) 0.821 (11)	484 (19) 0.854 (6)		1015 (104) 0.826 (16)				111 (6) 0.764 (10)
6650.517	241 (12) 0.358 (8)	196 (4) 0.822 (3)	480 (28) 0.848 (9)	435 (21) 0.872 (8)		865 (86) 0.811 (15)				189 (7) 0.748 (7)
6680.137	157 (19) 0.327 (19)									
6728.923		214 (6) 0.819 (5)								
6740.078		221 (7) 0.841 (6)	577 (52) 0.821 (14)	412 (26) 0.872 (10)						221 (15) 0.833 (11)
6749.27		262 (10) 0.811 (6)								
6764.596		226 (10) 0.822 (7)								
6812.330		208 (7) 0.811 (5)								
6816.004		258 (8) 0.813 (5)	484 (51) 0.827 (17)							
Nd III										
3597.628	137 (7) 0.484 (9)									
3603.983	185 (15) 0.472 (14)									

Table 3. continued.

Wavelength (Å)	HD 24712	HD 101065	HD 122970	HD 134214	HD 12932	HD 19918	HD 201601	HD 128898	HD 9289	HD 137949
3644.353	148 (9)									
	0.482 (10)									
4570.660							1013 (59)			
							0.676 (9)			
4759.526							779 (42)			
							0.712 (9)			
4769.622							802 (51)			
							0.686 (10)			
4796.499	212 (6)									
	0.439 (5)									
4821.986	209 (8)						1039 (74)			
	0.389 (6)						0.641 (11)			
4911.653							654 (33)			
							0.718 (8)			
4912.944	241 (8)									
	0.429 (5)									
4927.488	208 (7)									
	0.477 (6)									
5050.695			375 (11)		1058 (26)		583 (24)			92 (4)
			0.853 (5)		1.157 (4)		0.751 (7)			0.262 (8)
5084.660		203 (3)	454 (19)							
		0.828 (2)	0.852 (7)							
5127.044	163 (6)		398 (10)							86 (2)
	0.498 (6)		0.860 (4)							0.345 (5)
5151.731	215 (7)	227 (3)								29 (4)
	0.411 (5)	0.851 (2)								0.314 (26)
5203.924	159 (6)	251 (3)	465 (13)		948 (45)		474 (35)	373 (9)	447 (18)	128 (4)
	0.503 (6)	0.872 (2)	0.867 (5)		1.231 (8)		0.819 (12)	0.613 (4)	0.638 (7)	0.373 (5)
5286.753	267 (9)	268 (5)	498 (23)	541 (14)	918 (33)	717 (37)	845 (38)	933 (25)		28 (5)
	0.381 (6)	0.844 (3)	0.843 (7)	0.908 (4)	1.039 (6)	0.867 (8)	0.619 (7)	0.386 (4)		0.718 (30)
5294.113	188 (8)	303 (4)	432 (10)	198 (8)	872 (34)		541 (40)	298 (9)	601 (30)	138 (5)
	0.540 (7)	0.888 (2)	0.854 (4)	1.100 (7)	1.240 (6)		0.864 (12)	0.630 (5)	0.708 (8)	0.340 (7)
5410.099	213 (7)		392 (10)		841 (15)					47 (1)
	0.457 (5)		0.847 (4)		1.100 (3)					0.286 (6)
5566.015		169 (3)	363 (16)	340 (9)	781 (27)					26 (2)
		0.845 (3)	0.864 (7)	0.926 (5)	1.052 (6)					0.648 (17)
5633.554	241 (9)	238 (4)	492 (22)	486 (14)	1049 (36)	1070 (46)				16 (4)
	0.405 (6)	0.840 (3)	0.859 (7)	0.930 (5)	1.060 (6)	0.890 (7)				0.582 (46)
5677.179	236 (9)	164 (3)	442 (16)	421 (12)	1190 (39)	1160 (49)	901 (48)	565 (15)	572 (40)	52 (8)
	0.431 (6)	0.854 (4)	0.852 (6)	0.954 (5)	1.088 (5)	0.934 (7)	0.686 (9)	0.454 (4)	0.590 (11)	0.211 (26)
5802.532		220 (3)	511 (19)	441 (11)	1137 (34)	1055 (30)	869 (45)	503 (11)	640 (44)	66 (6)
		0.847 (3)	0.847 (6)	0.952 (4)	1.098 (5)	0.914 (5)	0.683 (8)	0.454 (4)	0.581 (11)	0.297 (16)
5845.020	227 (8)	275 (6)	483 (18)	369 (12)	1107 (32)	1072 (42)				65 (5)
	0.466 (6)	0.855 (4)	0.850 (6)	1.009 (6)	1.129 (6)	0.935 (6)				0.313 (12)
5851.542	261 (9)	277 (8)	461 (17)	462 (14)	1319 (49)	1267 (55)	863 (87)	547 (18)	663 (36)	65 (8)
	0.431 (6)	0.836 (5)	0.851 (6)	0.952 (5)	1.107 (6)	0.938 (7)	0.679 (16)	0.457 (5)	0.554 (9)	0.243 (20)
5987.683	245 (8)						692 (44)			
	0.464 (6)						0.730 (10)			
6145.068	194 (9)	197 (7)	266 (10)	226 (8)	1116 (38)	829 (32)		324 (12)	585 (43)	109 (8)
	0.482 (8)	0.857 (6)	0.856 (6)	1.015 (6)	1.144 (5)	0.982 (6)		0.518 (6)	0.624 (12)	0.270 (1)
6327.265				311 (10)		999 (56)		375 (15)	543 (55)	94 (7)
				1.030 (5)		0.971 (9)		0.514 (6)	0.628 (16)	0.248 (13)
6550.231				371 (12)	1310 (50)				657 (60)	102 (6)
				1.036 (5)	1.154 (6)				0.646 (15)	0.298 (9)
6690.830	235 (11)	227 (7)	481 (32)	469 (21)	1209 (96)	1295 (70)		761 (33)	445 (139)	40 (8)
	0.399 (8)	0.834 (5)	0.848 (11)	0.921 (7)	1.056 (13)	0.879 (9)		0.391 (7)	0.550 (49)	0.751 (34)
Eu II										
5818.746					515 (50)	482 (45)				
					0.940 (16)	0.721 (15)				
5872.978		136 (6)								
		0.786 (8)								
6049.513	74 (12)									
	0.243 (26)									
6173.029	79 (10)	75 (5)		82 (12)		364 (30)				
	0.248 (21)	0.800 (11)		0.570 (25)		0.736 (13)				
6303.423			84 (26)		555 (46)	356 (52)		145 (21)	282 (71)	
			0.788 (50)		0.950 (13)	0.740 (24)		0.164 (23)	0.423 (40)	
6437.640	109 (10)	57 (41)	109 (17)	117 (12)	662 (41)	469 (34)			525 (77)	151 (5)
	0.247 (14)	0.807 (11)	0.800 (26)	0.615 (17)	0.943 (10)	0.737 (12)			0.397 (23)	0.009 (6)
6645.110	110 (8)	38 (4)	105 (13)	172 (9)	600 (64)	489 (48)		227 (9)	300 (58)	191 (6)
	0.252 (12)	0.800 (18)	0.858 (20)	0.657 (8)	0.986 (17)	0.723 (16)		0.184 (6)	0.472 (31)	–0.001 (5)
Tb II										
6194.488		250 (56)								
		0.956 (35)								
Tb III										
5505.409	326 (19)		1129 (30)	501 (22)	1242 (31)			985 (17)	534 (28)	14 (2)
	0.884 (9)		0.957 (4)	1.404 (7)	1.228 (4)			0.864 (3)	0.675 (9)	0.543 (31)
5847.232	359 (23)		988 (33)	519 (30)				1150 (45)	474 (89)	103 (9)
	0.869 (10)		0.926 (5)	1.387 (9)				0.857 (6)	0.652 (30)	0.007 (15)
6092.897	218 (13)		991 (34)		677 (35)					140 (10)
	0.841 (10)		0.963 (6)		1.215 (8)					0.078 (12)

Amplitude (m s^{-1}) / Phase (period fraction)

Table 3. continued.

Wavelength (Å)	HD 24712	HD 101065	HD 122970	HD 134214	HD 12932	HD 19918	HD 201601	HD 128898	HD 9289	HD 137949
6323.620		654 (17) 1.119 (4)	1141 (51) 0.942 (7)	556 (45) 1.401 (13)	1124 (77) 1.237 (11)	507 (56) 1.109 (18)		965 (51) 0.826 (9)	495 (107) 0.799 (34)	202 (19) 0.038 (15)
6511.060	329 (23) 0.824 (11)	480 (11) 1.058 (4)			833 (75) 1.247 (14)	459 (45) 1.134 (16)			472 (117) 0.712 (41)	
6511.788		551 (13) 1.033 (4)			854 (67) 1.194 (13)	449 (57) 1.112 (20)				
6591.215			1022 (65) 0.977 (10)							
6687.698	197 (23) 0.846 (18)		913 (55) 0.936 (9)		1067 (227) 1.209 (34)	616 (146) 1.105 (38)				126 (18) −0.031 (23)
6716.566			913 (42) 0.932 (7)					1041 (175) 0.818 (26)		
6832.056		544 (19) 1.042 (6)								
Dy II										
3407.796	230 (14) 0.485 (10)									
3429.443	382 (24) 0.406 (10)									
3434.369	283 (14) 0.449 (8)									
3534.960	227 (13) 0.470 (9)									
3538.519	292 (14) 0.467 (8)									
3550.218	315 (19) 0.453 (10)									
3563.148	317 (18) 0.443 (9)									
3602.823	178 (39) 0.315 (35)									
4923.167	201 (13) 0.372 (11)									
5090.386			327 (23) 0.826 (11)							
5164.115				433 (31) 0.825 (11)						144 (12) 0.704 (14)
5169.688			356 (20) 0.843 (9)	368 (14) 0.841 (6)						84 (4) 0.785 (9)
5272.249		129 (3) 0.811 (4)								
5279.697		174 (4) 0.816 (4)								
5284.989		127 (3) 0.761 (5)								
5337.427		145 (6) 0.818 (7)								
5399.936		125 (6) 0.829 (8)								
5426.695			335 (45) 0.811 (21)	473 (25) 0.816 (9)		268 (66) 0.536 (39)				
5443.343		159 (6) 0.802 (7)								
5471.909		150 (4) 0.815 (5)				214 (99) 0.629 (70)				
5515.405		216 (5) 0.807 (4)								
5641.504		121 (6) 0.816 (8)								
5868.107			419 (57) 0.831 (22)							77 (14) 0.867 (30)
5924.558		120 (7) 0.837 (10)								
6196.234	160 (31) 0.329 (31)	230 (8) 0.798 (6)								
6654.228		161 (9) 0.830 (9)								124 (16) 0.837 (22)
6700.639	193 (30) 0.320 (24)		426 (68) 0.869 (25)	311 (52) 0.836 (27)						171 (23) 0.803 (22)
Dy III										
3919.398	278 (14) 0.490 (8)									
5730.284	255 (12) 0.451 (8)	129 (3) 0.838 (4)	403 (23) 0.848 (9)	496 (15) 0.893 (5)	683 (42) 1.068 (10)	705 (61) 0.866 (14)	356 (61) 0.671 (28)	856 (42) 0.413 (8)	461 (76) 0.518 (27)	39 (4) 0.446 (18)
Th III										
5376.130	39 (22) 1.120 (6)	388 (15) 1.088 (15)	670 (64) 1.425 (11)	273 (17)						186 (13) −0.111 (7)
6599.482	42 (19) 1.086 (9)	224 (13) 1.047 (23)	807 (120) 1.437 (21)	402 (53)						302 (12) 0.001 (7)